Assimilation of GOES-16 Satellite derived Winds into the Warn-on-Forecast System

Swapan Mallick[1,2] and Thomas A. Jones[1,2,3]

1. Cooperative Institute for Mesoscale Meteorological Studies, University of Oklahoma, Norman, OK
2. National Severe Storms Laboratory, Norman, OK
3. University of Oklahoma, Norman, OK

Submitted to: Atmospheric Research

Revised: May 21, 2020

Corresponding Author Address:
Dr. Thomas A. Jones
Cooperative Institute for Mesoscale Meteorological Studies
University of Oklahoma
and
NOAA/OAR/National Severe Storms Laboratory
120 David L. Boren Blvd.
Norman, OK 73072
E-mail: Thomas.Jones@noaa.gov

Abstract

The Advanced Baseline Imager (ABI) onboard the GOES-R series of geostationary satellites provides an opportunity to generate high-resolution satellite derived wind vectors over continental United States not possible from previous satellites. This study investigates the quality and the impact of assimilating satellite-derived winds (or Atmospheric Motion Vectors, AMVs) from the GOES-16 geostationary satellite on high-impact weather forecasts using the NOAA's ensemble based Warn-on-Forecast System (WoFS). The WoFS runs at convection allowing scales (~3 km) with a 15-minute cycling frequency assimilating all available observations including conventional, radar and GOES-16 cloud water path retrievals over a limited area domain. Four severe weather events during 2018 are considered in this study to assess the potential impacts of assimilating GOES-16 AMVs into the WoFS. A total of eight experiments performed, four that assimilate AMV data and the remaining four do not with all including conventional, radar, and other satellite data. This research represents the first step to assimilated high-resolution satellite derived winds into the convective-allowing ensemble data assimilation system. The results show that the overall impact of assimilation of AMVs is small, but positive for probabilistic forecasts of reflectivity objects.

Key words: GOES-R, Data Assimilation, Atmospheric Motion Vectors, Numerical Weather Prediction, Warn-on-Forecast.

1. Introduction

Satellite-derived wind speed and direction from cloud and moisture objects known as atmospheric motion vectors (AMVs) represent an approximation of the local wind at the height of the observed object (Velden et al. 1997). AMVs are an important and valuable data source for global as well as regional numerical weather prediction (NWP) models and analyses. AMVs mitigate critical data gaps in regions that are otherwise observation poor. It has been well established that numerical model analyses and forecasts benefit from the satellite-derived AMVs (Cardinali 2009; Santek 2010; Joo and Marriott 2013) and AMVs are routinely assimilated in all operational global NWP systems (Rohn et al. 2001; Le Marshall 2008a; Cotton and Forsythe 2012; Mallick et al. 2017). In particular, several studies also showed that assimilating AMVs improves the representation of tropical cyclone wind structure and its surrounding environmental flow fields in global NWP systems (Langland et al. 2009; Berger et al. 2011, Sears and Velden 2012).

While AMV datasets are adequate and reliable for global data assimilation systems, the coverage and processing methodologies are not optimized for smaller-scale phenomena. Regional data assimilation and forecasting systems are trending toward nested grids using convection permitting and even convection resolving scales. High-impact convective-scale events have important mesoscale flow fields that need to be resolved in order to improve these high-resolution analyses and forecasts (Stensrud et al. 2009, 2013; Madaus et al. 2014). The time has come to develop observation strategies that meet these increasing demands. The high-resolution AMV products from GOES-R have the potential to provide valuable information for regional NWP models, where the priority is the improved prediction of high impact weather events. These data sets are being realized through advancing satellite sensors and scanning strategies and improving AMV retrieval methodologies. Several studies found that assimilating high-resolution AMVs can benefit regional model forecasts of tropical cyclone track and intensity (e.g. Yamashita 2012, Velden et al., 2017, Elsberry et al. 2018, Kim and Kim 2018, Lim et al. 2019, Sawada et at. 2019). For example, Kim and Kim (2018) discuss the potential benefits and the effect of assimilating Himawari-8 AMVs on forecast errors in East Asia. For the observation system experiments, they used 3D-VAR data assimilation technique and the regional WRF model. The Japan Meteorological Agency (JMA) found that the assimilation of MTSAT rapid scan AMVs in their mesoscale model with four-dimensional variational data assimilation (4D-VAR) provided improvements to typhoon forecasts in the western Pacific (Yamashita 2012).

Le Marshall et al. (2008b) documented the impacts of high-resolution AMVs in the operational Australian regional model. Otsuka et al. (2015, 2018) and Kunii et al. (2016), conducted experiments assimilating rapid scan AMVs from Himawari-8 with a mesoscale regional model and the ensemble based Kalman filter data assimilation approach to forecast heavy rainfall events. Their results suggest that assimilating high resolution AMVs slightly increased the skill of wind and precipitation forecasts. However, research into whether or not assimilating AMVs improves forecasts of severe convection over land is much less advanced (Yesubabu et al. 2016).

The new GOES-R series of satellites include the Advanced Baseline Imager (ABI) which generates high resolution visible and infrared imagery from which additional products can be derived (Schmit et al. 2005, 2017). To develop the high-quality Level-2 (L2) derived products, the GOES-R algorithm working group (AWG) was formed (Daniels et al. 2008) with one key product being AMVs, also known as Derived Wind Motion observations (Velden et al. 2017). The improved performance of image-to-image navigation and registration due to the high spectral, temporal and special resolution of the ABI allows retrieval algorithms to extract more accurate

AMVs than previously possible (Velden et al. 2017). Previous studies (Wu et al. 2014, 2015) highlight the important contribution of high-resolution AMVs using GOES-R proxy datasets to mesoscale analyses. Their results suggest that high-resolution AMVs can improve model (WRF and HWRF) analyses and forecasts of TC intensity and structure. Recently, ECMWF documented their result on impact study with the GOES-16 AMVs using global assimilation experiments. The forecast impacts were generally neutral, but small reductions in the wind error at low levels and in the southern hemisphere were observed (Lean and Bormann 2019). Li et al. (2020) also show that the assimilation of the high-resolution AMVs from GOES-16 consistently improves the HWRF hurricane track and size forecasts, but have mixed impacts on intensity forecasts.

The goal of this research is to assess the impact of assimilating AMVs derived from GOES-16 ABI data into the Warn-on-Forecast System (WoFS) using four severe weather events from spring 2018. The initial quality of GOES-16 AMVs datasets is studied using different statistical methods including the number of observations available at each level and from each GOES-16 channel from which AMVs are retrieved. The observation innovation statistics are computed against the model background for quality assessment and to quantify the changes to the mesoscale environment within the model. This research represents the first step to assimilated satellite winds into the convective-allowing ensemble data assimilation system over land.

Following the Introduction, section 2 of this paper describes the satellite-derived wind products, the data assimilation and forecast system (WoFS), and the overall experiment design. Results of the impact of AMVs on the environment and reflectivity and updraft helicity (UH) forecasts are provided in section 3 with discussion and conclusions are present in section 4.

2. Data and Methods

2.1. GOES-R AMVs

Retrieval algorithms have been developed to estimate the direction and speed of identified cloud objects and/or moisture gradients in the atmosphere. In regional modeling applications, these retrievals can supplement radial velocity observations in radar coverage gaps and in non-precipitating regions. In addition, these data can add upper-level wind information where sounding and aircraft data are not assimilated. In this research, AMVs retrieved from GOES-R ABI visible and infrared channels are used, which exists at higher spatial and temporal resolutions than those from the previous generation imagers. These data are designed to address the needs of forecasters who rely observations of rapidly evolving phenomena to issue forecasts of potential high impact weather events (Lindsey et al. 2018, Zhang et al. 2019). The pixel resolution of the GOES-R ABI data has approximately 2 km for the infrared (IR), short wavelength infrared (SWIR) and water vapor (WV) bands and 0.5 km for the 0.64 μm visible band. A total of six channels are used for GOES-R AMV cloud and water vapor tracking whereas only four channels were used on GOES-13. Table 1 provides a summary of GOES-R ABI band number, wavelength, name and time interval used to derive AMVs.

Tracking features are used to generate the AMVs include cloud objects and the moisture gradients from three sequential ABI images. Visible band (0.64 μm) data is generated during the day time only. Emissive or infrared (IR) band product data is generated both day and night except for the 3.9-μm band, where product data is generated during the night only. Many improvements have been made in the AMVs retrieval algorithm used with ABI data. The algorithm for the GOES-N imager used long-established tracking and height assignment methods such as carbon dioxide

(CO_2) slicing or the water vapor intercept method (Nieman et al. 1997) and employs an auto-editor that includes an adjustment of the heights through minimization of a penalty function combining the observations with model background (Velden et al. 1998, Forsythe and Saunders 2008). The new algorithm developed for ABI data uses new tracking and height assignment techniques. An optimal estimation technique is used for the height assignment. The cloud height algorithm, which also allows for multi-layer cloud solutions, is used to derive cloud parameters including the cloud top height using multiple channels (Bresky et al. 2012, Heidinger 2013).

For target height assignment the GOES-R ABI channels 2, 7, 8 or 14 are used to track cloudy target scenes, pixel-level cloud-top pressures. The channels 8, 9, or 10 are used for targeting elevated moisture gradients (Daniels et al. 2012). The Sum of Squared difference (SSD, Euclidian distance), a correlation-based method is used to track cloud and clear-sky water vapor for the derivation of AMVs. To estimate the motion using cloud-top features, a tracking strategy called nested tracking is used. One of the uncertainties of the derived wind algorithm is the height assignment method. AMV retrievals rely on radiometric techniques for height assignment that have large uncertainties (Di Michele et al. 2013; Mueller et al. 2017). A study by Salonen et al. (2015) showed that the comparison of AMVs assigned heights with model analyses demonstrates AMVs model height differences that are consistent with the lidar results. Lean and Bormann (2019) conducted an experiment to estimate GOES-16 AMVs height assignment error contribution. Their results showed that height assignment error was around 70-90 hPa in the lowest level (800-1000 hPa), 120-170 hPa in the next level (600-800 hPa) and for high level, the error was around 40-60 hPa. This result suggests that the height error is near double in the 600-800 hPa level compared to lower and the upper levels. The comparison of AMVs heights with radiosonde profiles suggests that height assignment errors represent 70% of the overall uncertainty (Velden and Bedka 2009). Characterization and reduction of height assignment error continue to be aggressively investigated by the NWP community. The AMV community, in collaboration with cloud groups, are also actively trying to characterize the height assignment error. Full details of the GOES-R AMV retrieval algorithms can be found in the "GOES-R Advanced Baseline Imager (ABI) Algorithm Theoretical Basis Document for Derived Motion Winds" (Daniels et al. 2012; Heidinger 2013).

2.2. Initial Assessments of GOES-R AMV data and Quality Control

The GOES-R retrieved wind product file consists of wind vectors containing wind speed, location, wind direction, pressure height, brightness temperature and the corresponding quality control flags (QCF). In this study, AMVs data from GOES-East (16) are used. The raw L2 "DMWM1" files from NOAA/ NESDIS are downloaded from (https://thredds-test.unidata.ucar.edu/thredds/catalog/satellite/goes/east/Products/DerivedMotionWinds/catalog.html) in NetCDF file format. These data are available in realtime with a latency of only a few minutes making them very suitable for the WoFS or similar systems. Operational models generally use a post-processed and quality-controlled form of AMV data included in "prepbufr" files. However, these files only contain data at a much lower spatial and temporal resolution, making them inadequate for our purposes.

To determine which raw observations are suitable for assimilation, various quality control checks must be applied. All L2 AMV retrievals are assigned a unique quality control code (QCF) from 0-22. Figure 1 shows the percentage of AMVs observations with five different QCF for a typical time from 1800 UTC (mid-afternoon) to 0300 UTC (early evening) and for the four cases considered in this study. QCF-0 indicate the good data which account for less than 10% of all potential retrievals. The remaining QCF data are associated with a unique flag value from the number QCF-1 to QCF-22, which filtered out prior to the observation processing step used in this research. QCF-1 represents the data those are not pass QC because of the maximum gradient below acceptable threshold and QCF-3 failure because of cloud amount failure which occurs if the cloud cover is less than 10% for the cloud track winds or more than 0% cloud cover for water vapor clear-sky winds. QCF-4 is for median pressure failure, and the QCF-14 occurs when the median pressure used for the height assignment outside acceptable pressure range. For all the four cases, more than 60% of the potential retrievals are unused for the reason of cloud amount fail (QCF-3) or a non-valid the height assignment (QCF-14) (Fig. 1). Selection of only "good" retrievals represents the first QC step (QCS-1) of this research. For real-time AMV data processing all good quality retrievals within a -10 to +5-minute window from a particular analysis time are extracted from the raw L2 product files. At this stage, the wind speed (*ws*) and wind direction (*wd*) values are converted to the zonal and meridional velocity (*u, v*) components using the formula $u = ws*cos\ (90^0 + wd)$; $v = -ws*sin\ (90^0 + wd)$ for all retrievals which pass these steps.

In addition to the quality control checks built into the retrieval software, other quality control products exist. For example, a quality indicator (QI) is an intermediate product that defines the quality of good retrievals through comparisons with co-located radiosonde observations (e.g. Holmlund 1997; 1998). This product is used for quality control in the prepbufr files used in operational models, but was not available for this research. Many additional quality control methods used by various data assimilation centers are described in Santek et al. (2018). The authors' are aware that additional quality indictors will be required to fully optimize AMV assimilation into the WoFS.

The second stage of QC (QCS-2) is applied within the Grid-point Statistical Interpolation (GSI) software for all retrievals that pass QCS-1. First, GSI performs an outlier check. The innovation (*observation – background*) is calculated from the interpolated model background fields to the observed location. In case of AMV observations, the threshold value between the ratio of the innovation to the observation error is set to 5 by default. If the ratio is greater than 5 then AMVs data are not used. The other QCS-2 criteria are:

- Tropopause check for all wind data. Those with a pressure height less than 100 hPa
- Near Surface check. Those data having a pressure height greater than 950 hPa.
- No visible wind has been used with a pressure height above 700 hPa.
- No winds from the infrared longwave window having a pressure height in between 400-800 hPa.
- No upper level water vapor wind retrievals having a pressure height lower than 400 hPa.
- No AMV retrieval used having a direction departure greater than 50 degrees from the model analysis.
- No AMV retrieval used having a magnitude of wind speed outside the range 3-150 m s^{-1}.

Applying these quality control criteria (QCS-1 and QCS-2) results in approximately 75% of the potential infrared and 25% of the potential visible observations being filtered out and not assimilated into the system. The observation error for AMVs is calculated using suitable combinations the tracking error and the error in the speed (Bormann et al. 2003; Salonen and Bormann, 2013). It has been observed that for the IR bands from geostationary orbiting instruments, values ranging between 2.0 and 3.0 m s^{-1} are appropriate estimates (https://nwpsaf.eu/monitoring/amv/amvusage/mfmodel.html). As a result, the AMVs observation error was set to 2.0 m s^{-1} for the infrared bands and 1.5 m s^{-1} for the visible band.

2.3. Model configuration

The NOAA's ensemble based Warn-on-Forecast (WoF) project has developed a rapid-cycling, data assimilation and forecasting system to improve short-term (0-3 h) forecasts of high impact weather events (Stensrud et al. 2009; 2013). Since the beginning of the WoF project in 2009, continuous research and development in storm-scale data assimilation techniques has resulted in the creation of the NSSL's Warn-on-Forecast System (WoFS) (Wheatley et al. 2015; Jones et al. 2016; Skinner et al. 2016; Jones et al. 2018; Skinner et al. 2018; Gallo et al. 2018). The WoFS is a sub-hourly cycling, regional domain convective-scale ensemble data assimilation and forecast system that generates high impact weather forecasts including tornadoes, large hail, heavy rainfall, and landfalling tropical cyclones (Skinner et al. 2018; Yussouf and Knopfmeier 2019; Jones et al. 2019). Currently, the WoFS uses the Advanced Research version of the Weather Research and Forecasting Model (WRF-ARW) model core (Skamarock et al. 2008) coupled with the Grid-point Statistical Interpolation (GSI) package that includes an Ensemble Kalman Filter (EnKF) data assimilation system (Whitaker and Hamill 2002; Whitaker et al. 2008; DTC 2017, Liu et al. 2017).

The WoFS configuration used for these experiments similar to the one used for Hazardous Weather Testbed (HWT) operational testing beginning in 2017 and continuing through 2020. This version of the WoFS uses a 3-km horizontal grid spacing with 51 vertical levels and a model top at 20 hPa. The initial and boundary conditions are provided by an experimental 36-member High-

Resolution Rapid Refresh ensemble (HRRRe) (Benjamin et al. 2016; Alexander et al. 2018). The WoFS domain for these experiments is 250 x 250 grid points and is centered on the area of expected severe weather for each day. Ensemble spread is maintained by using a different set of planetary boundary layer and the radiation schemes for each ensemble member (Wheatley et al. 2015). In addition, all 36 members use the NSSL double moment cloud microphysics scheme (Mansell et al. 2010). GSI applies the QCF2 quality control step and calculates the ensemble priors to be used by the EnKF assimilation module. In the WoFS, separate sets of conventional observations, radar data, and satellite data are assimilated at 15-min intervals starting at 1800 UTC each day and ending at 0300 UTC the following day. See Jones et al. (2018) and Hu et al. (2019) for further information on the current WoFS configuration.

Assimilation of conventional, radar, and satellite observations provides the initial conditions of the convective features and the near-storm environment within the model analysis (Jones et al. 2015; Jones et al. 2018). In this research, the conventional data used include surface temperature, humidity, pressure and wind measurements from available Automated Surface Observing System (ASOS) sites and the Oklahoma Mesonet sites. Both radar reflectivity and radial velocity are assimilated into the WoFS and are derived from WSR-88D radar sites located within and near the experiment domain. WSR-88D reflectivity contained within the 1-km Multi-Radar Multi-Sensor (MRMS) product are objectively analyzed to a 5-km resolution from which observations to assimilate are drawn from (Smith et al. 2016). In case of clear-air reflectivity, the resolution is thinned to 10 km. The vertical height of the reflectivity observations used in the assimilation system ranges from 0.5 km to 10 km above ground level. Radial velocity is processed directly from level 2 WSR-88D data and also objectively analyzed to a 5-km resolution using the Cressman scheme. Satellite data in the form of cloud water path (CWP) retrievals from GOES-16 are assimilated during day time only (Jones et al. 2016). The GOES-16 CWP derived products represents the amount of cloud water and cloud ice present in an integrated column along with cloud height information (Minnis et al. 2011). CWP observations are generated using the Satellite ClOud and Radiation Property retrieval System (SatCORPS) developed by the NASA Langley research center and processed experimentally from GOES-16 data in real-time for WoF applications (Minnis et al. 2011, Jones et al. 2016). Both radar and CWP observations are generated at 15 minute intervals.

To limit the observation impact in the horizontal and the vertical direction, the covariance localization is used when updating the model state. The covariance localization information is used by the GSI-EnKF system for observation types assimilated including all conventional, radar and satellite CWP are similar to those used by Jones et al. (2018). For AMVs, they are set to 100 km for the horizontal and 0.8 scale height for the vertical localization (Table 2). The same localization values are used for both u and v wind components. An outlier threshold of 3.25 standard deviations from the mean is applied to all observation types within the EnKF code and those that fall outside this threshold are not assimilated to match the configuration used by the WoFS. To analyze the impact of GOES-16 AMV in the convective-scale ensemble data assimilation and forecasts, two sets of experiments are conducted for each case. One that assimilates AMV data (with AMV; WAMV) and one without AMV data (Control run; CNTL) with both assimilating all conventional, radar, and CWP observations.

2.4. Overviews of the selected cases

Four high impact weather events during the spring of 2018 are considered by this study to assess the potential impacts of assimilating GOES-16 AMVs into the WoFS. Each case contains a unique environment with different storm modes, but all generate numerous severe weather warnings and corresponding reports. The Storm Prediction Center (SPC) tornado, hail, and severe wind reports and the MRMS composite reflectivity within the domain of each event are provided in Figure 2 and Table 3.

On 2 May 2018, a slow-moving cold front initiated severe storms across Kansas (KS) and Oklahoma (OK) during the late afternoon and the evening producing significant wind damage across the region (Fig. 2a, Table 3). The environment ahead of the front was very unstable with adequate vertical wind shear for the development of isolated supercells. Several developed in southern OK and northern TX with the OK storm generating a few tornado reports (Fig. 2b). Convection in KS was more linear in nature, but still generated several tornados after 2300 UTC.

On 14 May, several areas of severe convection developed in TX, OK, and KS. The primary severe weather threats were hail and wind, but an isolated supercell did form in extreme southern KS that produced several tornadoes (Fig. 2c,d). Early afternoon convection across eastern CO and western KS produced a track of severe hail reports and generated outflow boundaries on which later KS convection initiated as it progressed eastward.

During the afternoon of 29 May 2018, a weakly capped and unstable airmass was present from central KS southward into western OK. By 2300 UTC, widespread severe convection had developed within the domain with several supercells presented from TX northward into KS (Fig. 2f). Long tracks of severe hail reports with a few tornadoes were produced by these supercells as they moved eastward (Fig. 2e).

During the late afternoon on 1 June 2018, a cold front was present in central Nebraska (NE) with a corridor of low-level moisture extending northward from NE into southeast South Dakota (SD). A severe linear mesoscale convective system (MCS) formed by 2300 UTC (Fig. 2h). This

MCS was moved to southeastward into southeast SD and northern NE producing multiple severe weather reports including 3 tornados and becoming primarily a severe wind threat as it moved into eastern NE (Fig. 2g, Table 3).

3. Results

3.1. AMVs Observation Statistics

In this section, the observation-space diagnostics including the number of observations assimilated and the observation innovation statistics for each assimilation cycle starting from 1800 UTC and ending at 0300 UTC the following day are calculated to assess the performance of the WoFS during the 9 hour continuous data assimilation period for each case. The spatial distribution of assimilated GOES-16 AMVs at 1800 UTC for the four cases examined in this study are shown over the model domain for each case (Fig. 3). The number of observations in three different range of pressure levels are the lower level (1000-700 hPa), middle level (700-400 hPa) and the upper level (400-100 hPa) are shown. It should be noted that the pressure levels of all the visible AMVs lie between 1000 to 700 hPa. A few AMVs from IR longwave window band (channel-14) are also retrieved within this layer (Fig. 4). The majority of IR winds are retrieved above 400 hPA and represent upper-level cirrus cloud movements. There are only a few (*or* no AMVs) assimilated in the mid-troposphere (700 – 400 hPa) due to much fewer water-vapor channel retrievals being present for these cases.

Figure 5 shows the percentage of AMVs assimilated at each 15-min assimilation cycle during the complete data assimilation period. The percentage is calculated between the total number of good AMVs (QCF-0) before the two stage of QC (QCS-1 and QCS-2) and the number of assimilated AMVs into WoFS within the study domain. The assimilated AMVs time series plots show the variation of the observations from VIS and IR channels. During the daytime hours, high resolution VIS AMVs are available for most data assimilation cycles for each case while WV and IR retrievals are more sparse, but are present for the entire cycling period.

On 2 May, 68% of potential AMV retrievals (out of total 14059) are assimilated, with the majority of those from the IR channels (Fig. 5a; Table 4). It is interesting to note that all IR observations are from 400-100 hPa level, no AMVs are assimilated in-between 700-400 hPa level. This may due to the fact that maximum number of AMVs are from IR longwave window (channel-14) and this AMVs having pressure in-between 400-800 hPa are fail GSI QC at QCS-2. For 14 May and 29 May, the number of available AMVs is much higher (almost double) compared to the number of AMVs on 2 May (Fig. 5b,c). Also, the vast majority of assimilated retrievals for the 14 29 May and 1 June cases are from the visible channel and not the IR channels. This is due to more extensive low-level cloud cover over the domains (not shown). Note that the number of visible retrievals decreases to zero between 0000 – 0100 UTC as darkness falls on each domain.

The quantitative and qualitative knowledge of observation innovation calculated from observation value minus background (O-B) is very important to determine the quality of the data assimilation system. The AMV observation innovation (O-B) is used in quality control, as well as the forecast implications. In each 15-minute assimilation cycle, AMV observation innovations are used to adjust the model fields to produce a more accurate and dynamically consistent analysis for a new forecast cycle. The total ensemble mean innovation of the eastward wind component (u-wind in m s^{-1}) is calculated from 1800 to 0300 UTC for each case (Fig. 6). The u-wind error variation at each assimilation cycle of the mean O-B lies between −2 and 2 m s^{-1} and the mean O-A lies between -1 and 1 m s^{-1} with the errors almost randomly distributed. The negative value indicate that the model background has a larger easterly wind component compared to GOES-16 AMVs observations. Results from the v-wind component are generally similar (not shown).

3.2. Wind analyses.

The observation diagnostics above indicate that the majority of wind speed increments are relatively small (< 2 m s^{-1}); however, there are some areas where the increments are much larger resulting in significant differences between the CNTL and WAMV experiments. To assess where these differences are largest, difference fields (WAMV – CNTL) of the ensemble mean wind speed at 4 different levels (500, 700, 850 hPa, and 500 m AGL) are computed at 2100 UTC for each case. On 2 May, the greatest difference in the environmental wind field occurs in eastern OK and southern KS at the 700 hPa level where WAMV increases wind speed more than 5 m s^{-1} (Fig. 7b). This region corresponds to an area where large numbers of visible channel AMV retrievals in OK and infrared retrievals in KS are assimilated (Fig. 3a). Environmental differences at other levels are generally small. Nearby ongoing convection, differences on the order of ±5 m s^{-1} are often apparent at all levels, but consistent patterns are difficult to discern. An exception occurs with the 850 hPa and 500 m wind speed differences associated with the western OK storms (Fig. 7c,d). Here, low-level wind speeds are generally greater in the WAMV experiment indicating the existence of more robust convection at this analysis time.

For the 14 May case, several differences between each experiment are also apparent. In the non-convective environment in OK, WAMV decreases windspeeds at 700 hPa and below in several areas by approximately 1-2 m s^{-1} (Fig. 8b-d.) Additionally, WAMV increases windspeed in the northwestern portion of the domain at 850 hPa and below while also increasing windspeed along the boundary in southern KS (Fig. 8c,d). This is due to a boundary being analyzed somewhat further north in WAMV compared to CNTL, which could have implications for convective initiation.

Several areas of windspeed differences also exist in the 29 May experiments. As before, differences at 500 hPa not associated with ongoing convection are small (Fig. 9a). However, much larger differences exist lower in the atmosphere. At 700 hPa and below, windspeed in western Oklahoma is 1-2 m s^{-1} lower in WAMV compared to CNTL (Fig, 9b-d). At 700 hPa, windspeed is increased more than 5 m s^{-1} over areas of western KS, indicating that WAMV analyzes stronger southwesterly flow in this region (Fig. 9c). Interestingly, WAMV decreases windspeed in the same area at 850 hPa and 500 m. WAMV also increases windspeed in northern TX corresponding to a convergence area associated with a deepening surface low and increases windspeeds associated with convection in north-central KS and southern NE (Fig. 9c,d).

Finally for the 1 June case, several areas where WAMV differs from CNTL are apparent. First, assimilating AMVs increases southerly windspeed at 700 hPa in central SD associated with developing convection (Fig. 10b). However, WAMV generates weaker winds below 700 hPa in western NE associated with a slightly slower eastward propagation of a dryline feature (Fig. 10b-d.) This decrease results in less dry air being advected into north-central NE where severe convection is developing. Overall, large scale impacts on the dynamical environment are relatively small, but there do exist regions where significant differences do exist especially at 700 hPa and below. These differences are often associated with boundaries, moisture transport, and convective characteristics, which will impact how high impact weather is forecast by this system.

3.3. Impact of AMVs on reflectivity forecasts.

Changes to the analyzed wind fields at various levels from assimilating AMVs impact the evolution of forecast convection in each experiment. These differences can be assessed by comparing forecast simulated radar reflectivity against observed reflectivity from the WSR-88D network. Forecasts initialized at 2100 UTC on 2 May show that both experiments accurately generate 0-90 minute forecasts of the eastward moving convection in southern KS (Fig. 11). Similarly, they both correctly forecast more isolated convection in OK while also having difficulty with the convection in far southwestern OK and north TX. However, more members from WAMV generate convection in this region by 2230 UTC compared to CNTL (Fig. 11e,f). This difference corresponds to the stronger windspeeds associated with the analyzed convection at the beginning of this forecast period at 2100 UTC (Fig. 7d.)

For forecasts initialized at 2100 UTC on 14 May, relatively few differences exist between CNTL and WAMV (Fig. 12). Both experiments have difficulty in correctly forecasting the evolution of the convective cells in KS while failing to forecast severe convection located on the KS – OK border despite the differences seen in the wind fields analyzed at the beginning of this forecast period. Larger differences between CNTL and WAMV are apparent for the 29 May case. At 2130 UTC, a severe storm is located along the KS-OK border moving northeastward that CNTL fails to forecast (Fig. 13a). This storm is depicted in WAMV and persists in that experiment out to 2230 UTC (Fig. 13f). Further north, neither experiment accurately depicts convection in central KS by 2130 UTC, but WAMV does begin to forecast convection in this area by 2200 UTC. This convection becomes well established in WAMV by 2230 UTC while still struggling to form in CNTL at this time (Fig. 13e,f). These differences are likely related to the slowdown in southerly winds in WAMV in western OK, though the exact physical relationship between this and its influence on the convection is unclear for this example.

Finally, significant differences between both experiments are also apparent for the 1 June case. At 2100 UTC, a complex of severe convection is moving eastward along the SD – NE border and intensifying. Forecasts initiated at this time from both experiments depict this convection and propagate it eastward, somewhat too quickly compared to observations. The key difference between CNTL and WAMV is that only the latter correctly forecasts the southern extent of the convection by 2230 UTC (Fig. 14e,f). WAMV also generates fewer false alarms further north compared to CNTL. Recall that southwesterly wind speed is decreased in WAMV, resulting in less dry air being advected into the pre-storm environment above the boundary layer. Thus, WAMV generates a more favorable environment for the development and persistence of convection which is indeed the result forecast.

Qualitatively, forecasts of convection are improved by assimilating AMVs in three out of the four examples shown. However, this assessment only represents a single forecast period for a particular case and more quantitative metrics are needed to fully assess the impact of assimilating AMVs.

3.4. Quantitative verification

The overall performance of AMV assimilation in the WoFS is assessed using an object-based verification method (Davis et al. 2006; Skinner et al. 2016; 2018) for all four cases. Model simulated ensemble mean composite reflectivity and 2-5 km Updraft Helicity (UH; Kain et al 2008) fields are compared to MRMS reflectivity and rotation objects (Newman et al. 2013) at each available forecast time step. A summary of total number of reflectivity and rotation objects accumulated for both WAMV and CNTL experiments and for each individual case is shown in

Table 5. The largest number of reflectivity and rotation objects are generated by the 14 and 29 May cases as they are associated with more widespread convection.

Performance diagrams (e.g. Roebber 2009) summarize the impact of AMVs for reflectivity (Fig. 15) and 2-5 km UH (Fig. 16) forecasts at 60-min, 90-min and 120-min forecasts times. These statistics are computed using all forecasts initiated from 1900 to 0300 UTC for each event. In the case of reflectivity, overall 60 to 120 minute forecast skill is similar for all experiments indicating that the differences observed in the examples shown above get washed out from the large number of objects where skill is unchanged between both experiments (Fig. 15). Slight forecast improvement is observed for 90 and 120 minute forecasts of the 14 May and 1 June events, while the impact of assimilating AMVs on the other two events is neutral (Fig. 15e-f, k-l). Differences are larger for 2-5 km UH verification, but not always in favor of WAMV. With the exception of 60 minute forecasts from the 1 June event, WAMV generates similar or slightly worse skill than the CNTL experiment. The largest difference occurs for the 14 May event, where WAMV consistently performed worse after 90 minutes (Fig. 16e). Interestingly, WAMV generates higher reflectivity skill for this case at the same times (Fig. 15e). Overall, most of the differences in skill are quite small and their statistical significance is marginal at best. Thus, while assimilating GOES-16 AMVs has the ability to substantially impact individual forecasts, the overall impact when analyzing all forecasts is neutral to positive for reflectivity and neutral to negative for 2-5 km UH. The different results for reflectivity and UH verification also highlight the difficulty in determining which set of experiments is truly the best.

4. Discussion and Conclusions

First part of this study investigates the quality of GOES-16 AMVs and the number of observations from different channels available for assimilation. The initial assessment showed that more than 60% of data are failed attempts at AMVs for the reason of cloud amount fail and height assignment. During the daytime the maximum number of observations are from VIS channels and only a few upper level AMVs are from IR channels. The results suggest that attention should be given to the quality as well as the quantities of the AMVs observation before assimilation into the high-resolution models.

The second part of this study investigated the direct impact of assimilating satellite-derived wind GOES-16 AMVs using the NOAA's WoFS on the high-impact weather forecasts. The results show the differences in the wind fields are generally confined to 700 hPa and below due to the limited number of upper-level AMVs assimilated. However, visible channel retrievals often modified the model wind-fields both in the large-scale environment and nearby developing convection. These differences led to differences in storm structure, moisture transport, and boundary location that impacted the forecasts of convection by the WoFS. Although the results suggest that the influence of GOES-16 AMVs on high-impact weather forecasts are neutral to positive in the case of reflectivity and neutral to negative in the case of 2-5 km UH, they seem to be case dependent. Our study is limited to 4 convective events during the May-June 2018, ongoing work on assessing the impact of assimilating AMVs is underway for spring 2019 and 2020 events. It is also important to identify the seasonal variation of the impact of AMVs including multiple assimilation system. The impacts of AMVs observations can vary depending on cloud interaction, observation time, observation errors and land surface properties. Although studies have shown that AMVs can increase skill in NWP, the issues related to quality control and height assignment remain. A good specification of the AMVs observation error information that is crucial for data assimilation has made difficult due to its complex natures. More study is needed to address these series of issues. Other future research could be similar to the impact study of high-resolution AMVs from GOES-R for hurricanes forecasts (Velden et al. 2017, Li et al. 2020). With high-resolution GOES-R AMVs data research work can extend to see the model impact for storm-scale structure changes and identification sever storm. This research represents the first step to assimilated GOES-16 AMVs into the high-resolution limited area model and the results of this study provide guidance for the use of GOES-16 AMVs into the convective-allowing ensemble data assimilation system. Despite the sometimes-mixed impacts, there are good lessons to be learned from this investigation. To maximize the effect of assimilating GOES-16 AMVs on the high-resolution limited model forecasts, additional studies are needed using various assimilation and forecast systems

Acknowledgments

Funding for this research was provided by NASA ROSES NNX15AR57G with additional support provided by the NOAA/Office of Oceanic and Atmospheric Research under NOAA–University of Oklahoma Cooperative Agreement NA16OAR4320115, under the U.S. Department of Commerce. CWP observations were derived from the SAT-CORPS product generated by NASA Langley Research Center. This work would also not be possible without the support of the entire Warn-on-Forecast team.

References:

Alexander, C. R., and Coauthors, 2018: Development of the High Resolution Rapid Refresh Ensemble (HRRRE). 22nd Conf. on Integrated Observing and Assimilation Systems for the Atmosphere, Oceans, and Land Surface, Austin, TX, Amer. Meteor. Soc., 11.3, https://ams.confex.com/ams/98Annual/webprogram/Paper335526.html.

Benjamin, S. G., and Coauthors, 2016: A North American hourly assimilation and model forecast cycle: The Rapid Refresh. Mon. Wea. Rev., 144, 1669–1694, https://doi.org/10.1175/MWR-D-15-0242.1

Berger, H., R. Langland, C.S. Velden, C.A. Reynolds, and P.M. Pauley, 2011: Impact of Enhanced Satellite-Derived Atmospheric Motion Vector Observations on Numerical Tropical Cyclone Track Forecasts in the Western North Pacific during TPARC/TCS-08. *J. Appl. Meteor. Climatol.,* **50**, 2309–2318, https://doi.org/10.1175/JAMC-D-11-019.1

Bormann, N., S. Saarinen, G. Kelly, and J. Thépaut, 2003: The Spatial Structure of Observation Errors in Atmospheric Motion Vectors from Geostationary Satellite Data. *Mon. Wea. Rev.,* **131**, 706–718, https://doi.org/10.1175/1520-0493(2003)131<0706:TSSOOE>2.0.CO;2

Bresky, W.C., J.M. Daniels, A.A. Bailey, and S.T. Wanzong, 2012: New Methods toward Minimizing the Slow Speed Bias Associated with Atmospheric Motion Vectors. *J. Appl. Meteor. Climatol.,* **51**, 2137–2151, https://doi.org/10.1175/JAMC-D-11-0234.1

Cardinali, C., 2009: Forecast sensitivity to observation (FSO) as a diagnostic tool. ECMWF Tech. Memo. 599, 26 pp.

Cotton, J., Forsythe, M., (2012): AMVs at the Met Office: activities to improve their impact in NWP. Proceedings of the 12th International Winds Workshop, Auckland.

Daniels, J., W. Bresky, C. Velden, I. Genkova, S. Wanzong, and H. Berger, 2008: Algorithm and software development of atmospheric motion vector (AMV) products for the future GOES-R Advanced Baseline Imager. *Proc. Ninth Int. Winds Workshop*, Annapolis, MD, EUMETSAT. [Available online at http://cimss.ssec.wisc.edu/iwwg/workshop9/ext_abstracts/5.%20Daniels_Algorithm%20adn%20software%20development%20of%20AMV%20products%20for%20the%20future%20GOES-R%20ABI.pdf.]

Daniels, J., Bresky, W., Wanzong, S., Velden, C., Berger, H., July 2012. GOES-R Advanced Baseline Imager (ABI) Algorithm Theoretical Basis Document for Derived Motion Winds, Version 2.5. available https://www.star.nesdis.noaa.gov/goesr/docs/ATBD/DMW.pdf.

Davis, C., B. Brown, and R. Bullock, 2006: Object-Based Verification of Precipitation Forecasts. Part I: Methodology and Application to Mesoscale Rain Areas. *Mon. Wea. Rev.,* **134**, 1772–1784, https://doi.org/10.1175/MWR3145.1

Developmental Testbed Center, 2017: Gridpoint Statistical Interpolation Advanced User's Guide Version 3.6.0.0. Available at http://www.dtcenter.org/com-GSI/users/docs/index.php, 143 pp.

Di Michele, S., T. McNally, P. Bauer and I. Genkova, "Quality Assessment of Cloud-Top Height Estimates From Satellite IR Radiances Using the CALIPSO Lidar," in *IEEE Transactions on Geoscience and Remote Sensing*, vol. 51, no. 4, pp. 2454-2464, April 2013. doi: 10.1109/TGRS.2012.2210721

Elsberry, R.L., E.A. Hendricks, C.S. Velden, M.M. Bell, M. Peng, E. Casas, and Q. Zhao, 2018: Demonstration with Special TCI-15 Datasets of Potential Impacts of New-Generation Satellite Atmospheric Motion Vectors on Navy Regional and Global Models. *Wea. Forecasting,* **33**, 1617–1637, https://doi.org/10.1175/WAF-D-17-0168.1

Forsythe, M., Saunders, R., 2008. Third analysis of the data displayed on the NWP SAF AMV monitoring website. Available online at https://nwpsaf.eu/site/monitoring/winds-quality-evaluation/amv/amvanalysis-reports/.

Heidinger, A. K., 2013: ABI cloud height. NOAA NESDIS Center for Satellite Applications and Research Algorithm Theoretical Basis Doc., 79 pp. [Available online at https://www.star.nesdis.noaa.gov/goesr/docs/ATBD/Cloud_Height.pdf]

Holmlund K. 1997: Quality Indicators for Atmospheric Motion Vectors: Reliability and Impact on the EUMETSAT Product Generation. *Proc. Meteorological Data Users' Conference,* Brussels, Belgium, EUMETSAT, 355-362.

Holmlund K., 1998: The Utilization Of Statistical Properties of Satellite-Derived Atmospheric Motion Vectors to Derive Quality Indicators. *Wea. Forecasting,* 13, 1093-1104.

Hu, J., N. Yussouf, D.D. Turner, T.A. Jones, and X. Wang, 2019: Impact of Ground-Based Remote Sensing Boundary Layer Observations on Short-Term Probabilistic Forecasts of a Tornadic Supercell Event. *Wea. Forecasting,* **34**, 1453–1476, https://doi.org/10.1175/WAF-D-18-0200.1

Jones, T. A., D. J. Stensrud, L. Wicker, P. Minnis, and R. Palikonda, 2015: Simultaneous radar and satellite data storm-scale assimilation using an ensemble Kalman filter approach for 24 May 2011. Mon. Wea. Rev., 143, 165–194, https:// doi.org/10.1175/MWR-D-14-00180.1.

Jones, T. A., K. Knopfmeier, D. Wheatley, G. Creager, P. Minnis, and R. Palikonda, 2016: Storm-scale data assimilation and ensemble forecasting with the NSSL Experimental Warn on-Forecast System. Part I: Combined radar and satellite assimilation. Wea. Forecasting, 31, 297–327, https://doi.org/ 10.1175/WAF-D-15-0107.1.

Jones, T. A., X. Wang, P. Skinner, A. Johnson, and Y. Wang, 2018: Assimilation of GOES-13 Imager clear-sky water vapor (6.5 mm) radiances into a Warn-on-Forecast system. Mon. Wea. Rev., 146, 1077–1107, https://doi.org/10.1175/MWR-D-17-0280.1.

Jones, T. A., P. Skinner, K. Knopfmeier, E. Mansell, P. Minnis, R. Palikonda, and W. Smith, 2018: Comparison of Cloud Microphysics Schemes in a Warn-on-Forecast System Using Synthetic Satellite Objects. *Wea. Forecasting,* **33**, 1681–1708, https://doi.org/10.1175/WAF-D-18-0112.1

Jones, T. A, P. Skinner, N. Yussouf, K. Knopfmeier, A. Reinhart, and D. Dowell, 2019: Forecasting High-Impact Weather in Landfalling Tropical Cyclones Using a Warn-on-Forecast System. *Bull. Amer. Meteor. Soc.,* **100**, 1405–1417, https://doi.org/10.1175/BAMS-D-18-0203.1

Joo, S., J. Eyre, and R. Marriott, 2013: The Impact of MetOp and Other Satellite Data within the Met Office Global NWP System Using an Adjoint-Based Sensitivity Method.*Mon. Wea. Rev.,* 141, 3331 3342, https://doi.org/10.1175/MWR-D-12-00232.1

Kain, J.S., S.J. Weiss, D.R. Bright, M.E. Baldwin, J.J. Levit, G.W. Carbin, C.S. Schwartz, M.L. Weisman, K.K. Droegemeier, D.B. Weber, and K.W. Thomas, 2008: Some Practical Considerations Regarding Horizontal Resolution in the First Generation of Operational Convection-Allowing NWP. *Wea. Forecasting,* **23**, 931–952, https://doi.org/10.1175/WAF2007106.1

Kim, D. and H.M. Kim, 2018: Effect of Assimilating Himawari-8 Atmospheric Motion Vectors on Forecast Errors over East Asia. *J. Atmos. Oceanic Technol.,* **35**, 1737–1752,https://doi.org/10.1175/JTECH-D-17-0093.1

Kunii, M., M. Otsuka, K. Shimoji, and H. Seko, 2016: Ensemble data assimilation and forecast experiments for the September 2015 heavy rainfall event in Kanto and Tohoku Regions with atmospheric motion vectors from Himawari-8. *SOLA*, **12**, 209–214.

Langland, R.H., C. Velden, P.M. Pauley, and H. Berger, 2009: Impact of Satellite-Derived Rapid-Scan Wind Observations on Numerical Model Forecasts of Hurricane Katrina. *Mon. Wea. Rev.,* **137**, 1615–1622, https://doi.org/10.1175/2008MWR2627.1

Lean, K. and N. Bormann, 2019: "Moving to GOES-16: a new generation of GOES AMVs". ECMWF report. Available at [https://www.ecmwf.int/node/18860], DOI: 10.21957/2ryh9v5no

Le Marshall, J., J. Jung, T. Zapotocny, C. Redder, M. Dunn, J. Daniels, and L. P. Riishojgaard, 2008a: Impact of MODIS atmospheric motion vectors on a global NWP system. *Aust. Meteor. Mag.*, **57**, 45-51.

Le Marshall, J., R. Seecamp, M. Dunn, C. Velden, S. Wanzong, K. Puri, R. Bowen, and A. Rea, 2008b: The contribution of locally generated MTSat-1R atmospheric motion vectors to operational meteorology in the Australian region. *Aust. Meteor. Mag.,* **57**, 359-365.

Li, J., J. Li, C. Velden, P. Wang, T. Schmit, J. Sippel, 2020; Impact of rapid-scan-based dynamical information over the inner-core region of hurricanes from GOES-16 ABI on HWRF hurricane track forecasts. *JGR*. https://doi.org/10.1029/2019JD031647

Lim, A.H., J.A. Jung, S.E. Nebuda, J.M. Daniels, W. Bresky, M. Tong, and V. Tallapragada, 2019: Tropical Cyclone Forecasts Impact Assessment from the Assimilation of Hourly Visible, Shortwave, and Clear-Air Water Vapor Atmospheric Motion Vectors in HWRF. *Wea. Forecasting,* **34**, 177–198, https://doi.org/10.1175/WAF-D-18-0072.1

Lindsey, D.T., D. Bikos, and L. Grasso, 2018: Using the GOES-16 Split Window Difference to Detect a Boundary prior to Cloud Formation. *Bull. Amer. Meteor. Soc.,* **99**,1541–1544, https://doi.org/10.1175/BAMS-D-17-0141.1

Liu, H., M. Hu, D. Stark, H. Shao, G. Ge, K. Newman, and J. Whitaker, 2017: Ensemble Kalman Filter (EnKF) User's Guide Version 1.2. Developmental Testbed Center. Available at http://www.dtcenter.org/EnKF/users/docs/index.php, 80 pp.

Madaus, L.E., G.J. Hakim, and C.F. Mass, 2014: Utility of Dense Pressure Observations for Improving Mesoscale Analyses and Forecasts. *Mon. Wea. Rev.,* **142**, 2398–2413, https://doi.org/10.1175/MWR-D-13-00269.1

Mallick, S., D. Dutta, and K.-H. Min, 2017: Quality assessment and forecast sensitivity of global remote sensing observations. *Adv. Atmos. Sci.*, **34**(3), 371–382, doi:10.1007/s00376-016-6109-8.

Mansell, E.R., C.L. Ziegler, and E.C. Bruning, 2010: Simulated Electrification of a Small Thunderstorm with Two-Moment Bulk Microphysics. *J. Atmos. Sci.,* **67**, 171–194,https://doi.org/10.1175/2009JAS2965.1

Minnis, P., and Coauthors, 2011: CERES Edition-2 cloud property retrievals using TRMM VIRS and Terra and Aqua MODIS data, Part I: Algorithms. *IEEE Trans. Geosci. Remote Sens.*, **49**, 4374–4400, doi:https://doi.org/10.1109/TGRS.2011.2144601.

Mueller, K.J., D.L. Wu, Á. Horváth, V.M. Jovanovic, J. Muller, L. Di Girolamo, M.J. Garay, D.J. Diner, C.M. Moroney, and S. Wanzong, 2017: Assessment of MISR Cloud Motion Vectors (CMVs) Relative to GOES and MODIS Atmospheric Motion Vectors (AMVs). *J. Appl. Meteor. Climatol.,* **56**, 555–572, https://doi.org/10.1175/JAMC-D-16-0112.1

Newman, J.F., V. Lakshmanan, P.L. Heinselman, M.B. Richman, and T.M. Smith, 2013: Range-Correcting Azimuthal Shear in Doppler Radar Data. *Wea. Forecasting,* **28**,194–211, https://doi.org/10.1175/WAF-D-11-00154.1

Nieman, S.J., W.P. Menzei, C.M. Hayden, D. Gray, S.T. Wanzong, C.S. Velden, and J. Daniels, 1997: Fully Automated Cloud-Drift Winds in NESDIS Operations. *Bull. Amer. Meteor.Soc.,* **78**, 1121–1134, https://doi.org/10.1175/1520-0477(1997)078<1121:FACDWI>2.0.CO;2

Otsuka, M., M. Kunii, H. Seko, K. Shimoji, M. Hayashi, and K. Yamashita, 2015: Assimilation experiments of MTSAT rapid scan atmospheric motion vectors on a heavy rainfall event. *J. Meteor. Soc. Japan*, **93**, 459– 475.

Otsuka, M.; Seko, H.; Shimoji, K.; Yamashita, K., 2018, Characteristics of Himawari—8 Rapid Scan Atmospheric Motion Vectors Utilized in Mesoscale Data Assimilation. *J. Meteorol. Soc. Jpn.* **2018**, *96B*, 111–131.

Roebber, P. J., 2009: Visualizing multiple measures of forecast quality. Wea. Forecasting, 24, 601–608, https://doi.org/10.1175/ 2008WAF2222159.1.

Rohn, M., G. Kelly, and R.W. Saunders, 2001: Impact of a New Cloud Motion Wind Product from Meteosat on NWP Analyses and Forecasts. *Mon. Wea. Rev.,* 129, 2392–2403, https://doi.org/10.1175/1520-0493(2001)129<2392:IOANCM>2.0.CO;2

Salonen, K. and N. Bormann, 2013. Winds of change in the use of Atmospheric Motion Vectors in the ECMWF system. ECMWF Newsletter 136, 23–27.

Salonen, K., J. Cotton, N. Bormann, and M. Forsythe, 2015: Characterizing AMV Height-Assignment Error by Comparing Best-Fit Pressure Statistics from the Met Office and ECMWF Data Assimilation Systems. *J. Appl. Meteor. Climatol.,* **54**, 225–242, https://doi.org/10.1175/JAMC-D-14-0025.1

Santek, D., 2010: The Impact of Satellite-Derived Polar Winds on Lower-Latitude Forecasts. *Mon. Wea. Rev.,* 138, 123–139, https://doi.org/10.1175/2009MWR2862.1

Sawada, M., Z. Ma, A. Mehra, V. Tallapragada, R. Oyama, and K. Shimoji, 2019: Impacts of Assimilating High-Resolution Atmospheric Motion Vectors Derived from Himawari-8 on Tropical Cyclone Forecast in HWRF. *Mon. Wea. Rev.,* **147**, 3721–3740, https://doi.org/10.1175/MWR-D-18-0261.1

Schmit, T. J., M. M. Gunshor, W. P. Menzel, J. Li, S. Bachmeier, and J. J. Gurka, 2005: Introducing the next-generation Ad- vanced Baseline Imager (ABI) on GOES-R. Bull. Amer. Meteor. Soc., 86, 1079–1096, doi:10.1175/BAMS-86-8-1079.

Schmit, T.J., P. Griffith, M.M. Gunshor, J.M. Daniels, S.J. Goodman, and W.J. Lebair, 2017: A Closer Look at the ABI on the GOES-R Series. *Bull. Amer. Meteor. Soc.,* **98**, 681–698, https://doi.org/10.1175/BAMS-D-15-00230.1

Sears, J. and C.S. Velden, 2012: Validation of Satellite-Derived Atmospheric Motion Vectors and Analyses around Tropical Disturbances. *J. Appl. Meteor. Climatol.,* **51**,1823–1834, https://doi.org/10.1175/JAMC-D-12-024.1

Skamarock, W. C., and Coauthors, 2008: A description of the Advanced Research WRF version 3. NCAR Tech. Note NCAR/TN-4751STR, 113 pp., https://dx.doi.org/10.5065/D68S4MVH.

Skinner, P.S., D.M. Wheatley, K.H. Knopfmeier, A.E. Reinhart, J.J. Choate, T.A. Jones, G.J. Creager, D.C. Dowell, C.R. Alexander, T.T. Ladwig, L.J. Wicker, P.L. Heinselman, P. Minnis, and R. Palikonda, 2018: Object-Based Verification of a Prototype Warn-on-Forecast System. *Wea. Forecasting,* **33**, 1225–1250, https://doi.org/10.1175/WAF-D-18-0020.1

Skinner, P.S., L.J. Wicker, D.M. Wheatley, and K.H. Knopfmeier, 2016: Application of Two Spatial Verification Methods to Ensemble Forecasts of Low-Level Rotation. *Wea. Forecasting,* **31**, 713–735, https://doi.org/10.1175/WAF-D-15-0129.1

Smith, T. M., and Coauthors, 2016: Multi-Radar Multi-Sensor (MRMS) severe weather and aviation products: Initial operating capabilities. *Bull. Amer. Meteor. Soc.*, **97**, 1617–1630, https://doi.org/10.1175/BAMS-D-14-00173.1.

Stensrud, D.J., M. Xue, L.J. Wicker, K.E. Kelleher, M.P. Foster, J.T. Schaefer, R.S. Schneider, S.G. Benjamin, S.S. Weygandt, J.T. Ferree, and J.P. Tuell, 2009: Convective-Scale Warn-on-Forecast System. *Bull. Amer. Meteor. Soc.,* **90**, 1487–1500, https://doi.org/10.1175/2009BAMS2795.1

Stensrud, D. J., and Coauthors, 2013: Progress and challenges with Warn-on-Forecast. Atmos. Res., 123, 2-16, https://doi.org/10.1016/j.atmosres.2012.04.004.

Velden, C.S., C.M. Hayden, S.J. Nieman, W. Paul Menzel, S. Wanzong, and J.S. Goerss, 1997: Upper-Tropospheric Winds Derived from Geostationary Satellite Water Vapor Observations. *Bull. Amer. Meteor. Soc.,* **78**, 173–196, https://doi.org/10.1175/1520-0477(1997)078<0173:UTWDFG>2.0.CO;2

Velden, C.S., T.L. Olander, and S. Wanzong, 1998: The Impact of Multispectral GOES-8 Wind Information on Atlantic Tropical Cyclone Track Forecasts in 1995. Part I: Dataset Methodology, Description, and Case Analysis. *Mon. Wea. Rev.,* **126**, 1202–1218, https://doi.org/10.1175/1520-0493(1998)126<1202:TIOMGW>2.0.CO;2

Velden, C.S. and K.M. Bedka, 2009: Identifying the Uncertainty in Determining Satellite-Derived Atmospheric Motion Vector Height Attribution. *J. Appl. Meteor. Climatol.,* **48**,450–463, https://doi.org/10.1175/2008JAMC1957.1

Velden, C., W.E. Lewis, W. Bresky, D. Stettner, J. Daniels, and S. Wanzong, 2017: Assimilation of High-Resolution Satellite-Derived Atmospheric Motion Vectors: Impact on HWRF Forecasts of Tropical Cyclone Track and Intensity. *Mon. Wea. Rev.,* **145**, 1107–1125, https://doi.org/10.1175/MWR-D-16-0229.1

Wheatley, D. M., K. H. Knopfmeier, T. A. Jones, and G. J. Creager, 2015: Storm-scale data assimilation and ensemble forecasting with the NSSL Experimental Warn-on-Forecast System. Part I: Radar data experiments. Wea. Forecasting, 30, 1795–1817, https://doi.org/10.1175/WAF-D-15-0043.1.

Whitaker, J.S. and T.M. Hamill, 2002: Ensemble Data Assimilation without Perturbed Observations. *Mon. Wea. Rev.,* **130**, 1913–1924, https://doi.org/10.1175/1520-0493(2002)130<1913:EDAWPO>2.0.CO;2

Whitaker, J.S., T.M. Hamill, X. Wei, Y. Song, and Z. Toth, 2008: Ensemble Data Assimilation with the NCEP Global Forecast System. *Mon. Wea. Rev.,* **136**, 463–482,https://doi.org/10.1175/2007MWR2018.1

Wu, T., H. Liu, S. Majumdar, C. Velden, J. Anderson, 2014: Influence of assimilating satellite-derived atmospheric motion vector observations on numerical analyses and forecasts of tropical cyclone track and intensity. *Mon. Weather Rev.*, **142,** 49–71.

Wu, T., C. Velden, S. Majumdar, H. Liu, J. Anderson, 2015: Understanding the influence of assimilating subsets of enhanced atmospheric motion vectors on numerical analyses and forecasts of tropical cyclone track and intensity with an ensemble Kalman Filter. *Mon. Weather Rev.*, **143**, 2506–2531.

Yamashita, K., 2012: An observing system experiment of MTSAT rapid scan AMV using JMA meso-scale operational NWP system. Proc. 11th Int. Winds Workshop, Auckland, New Zealand, IWWG, IWW11. [Available online at http://cimss.ssec.wisc.edu/iwwg/iwwg_meetings.html.]

Yesubabu V, Srinivas CV, Langodan S, Hoteit I (2016) Predicting extreme rainfall events over Jeddah, Saudi Arabia: Impact of data assimilation with conventional and satellite observations. Q J R Meteorol Soc 142(694):327–348. https://doi.org/10.1002/qj.2654

Yussouf, N. and K. H. Knopfmeier; 2019 Application of Warn-on-Forecast System for Flash-Flood Producing Heavy Convective Rainfall Events. Doi: https://doi.org/10.1002/qj.3568

Zhang, F., M. Minamide, R.G. Nystrom, X. Chen, S. Lin, and L.M. Harris, 2019: Improving Harvey forecasts with next-generation weather satellites. *Bull. Amer. Meteor. Soc.,* **0**, https://doi.org/10.1175/BAMS-D-18-0149.1

Tables

(Channel No.)	Approx. Central Wavelength (µm)	Wavelength Range (µm)	Image Time Interval (mins)	Pixel resolution (km)	Band Type	Band Nickname
2	0.64	0.59-0.69	5	0.5	Visible	Red
7	3.9	3.80-4.00	5	2	Infrared	Shortwave Window
8	6.2	5.77-6.6	5	2	Infrared	Upper-Level Tropospheric Water Vapor
9	6.9	6.75-7.15	5	2	Infrared	Mid-Level Tropospheric Water Vapor
10	7.3	7.24-7.44	5	2	Infrared	Lower-level Water Vapor
14	11.2	10.8-11.6	5	2	Infrared	Longwave Window

Table 1. Summary of GOES-16 ABI band number, wavelength, name and time interval used to derive AMVs.

Observation Type	Variables	Horizontal localization (km)	Vertical Localization [$\ln(p/p_{ref})$]	Observation Error
Mesonet	Eastward (*u*-) wind	60	0.85	1.75 m s $^{-1}$
	Northward (*v*-) wind	60	0.85	1.75 m s $^{-1}$
	Temperature (*T*)	60	0.85	1.75 K
	Dewpoint (T_d)	60	0.85	2.0 K
	Pressure (*Ps*)	60	0.85	1.5 hPa
Radar	Reflectivity (*dBZ*)	18	0.80	5.0 dBZ
	Radial velocity (*RW*)	18	0.80	3.0 m s $^{-1}$
Satellite (GOES-16)	Cloud water path (*CWP*)	36	1.05	0.025 - 0.15 kg m $^{-2}$
	AMVs (*u*-wind)	100	0.80	1.5 m s $^{-1}$ for VIS 2.0 m s $^{-1}$ for IR
	AMVs (*v*-wind)	100	0.80	1.5 m s $^{-1}$ for VIS 2.0 m s $^{-1}$ for IR

Table 2. List of the observation type, horizontal and vertical covariance localization length scale and the observations error used by the WoFS system. Errors are similar to those used by Jones et al. (2018).

Event	Tornadoes	Hail	Wind
2 May, 2018	16	44	97
14 May, 2018	4	98	46
29 May, 2018	6	112	47
1 June, 2018	3	31	46

Table 3. Total number of tornado, severe hail (diameter > 1.0 in.), and severe-wind (wind speed > = 58 mph) reports within the model domain for each case consider in this study. The total number is counted over the study domain between the time 1800 and 0500 UTC the following day.

Event	Total Number of AMVs (Before QC)	Percentage (%) of AMVs used in DA.		
		ALL	VIS Band	IR Band
2 May, 2018	14059	68	28	40
14 May, 2018	22723	78	67	11
29 May, 2018	22645	72	55	17

1 June, 2018	6867	86	77	8
Average	16574	76	57	19

Table 4. Summary of the total number of good retrievals used before and after assimilation over the study domain.

Event	dBZ		Rotation	
	CNTL	WAMV	CNTL	WAMV
2 May, 2018	77741	81599	33335	33759
14 May, 2018	120896	120280	49388	44771
29 May, 2018	124263	129505	46230	41893
1 June, 2018	74778	74792	30871	30085
Total	397678	406176	159824	150508

Table 5. Summary of total number of reflectivity and rotation objects accumulated over all the ensemble member and 180-min forecasts times for both CNTL and WAMV experiments and for all the four cases over the study domain.

Figures

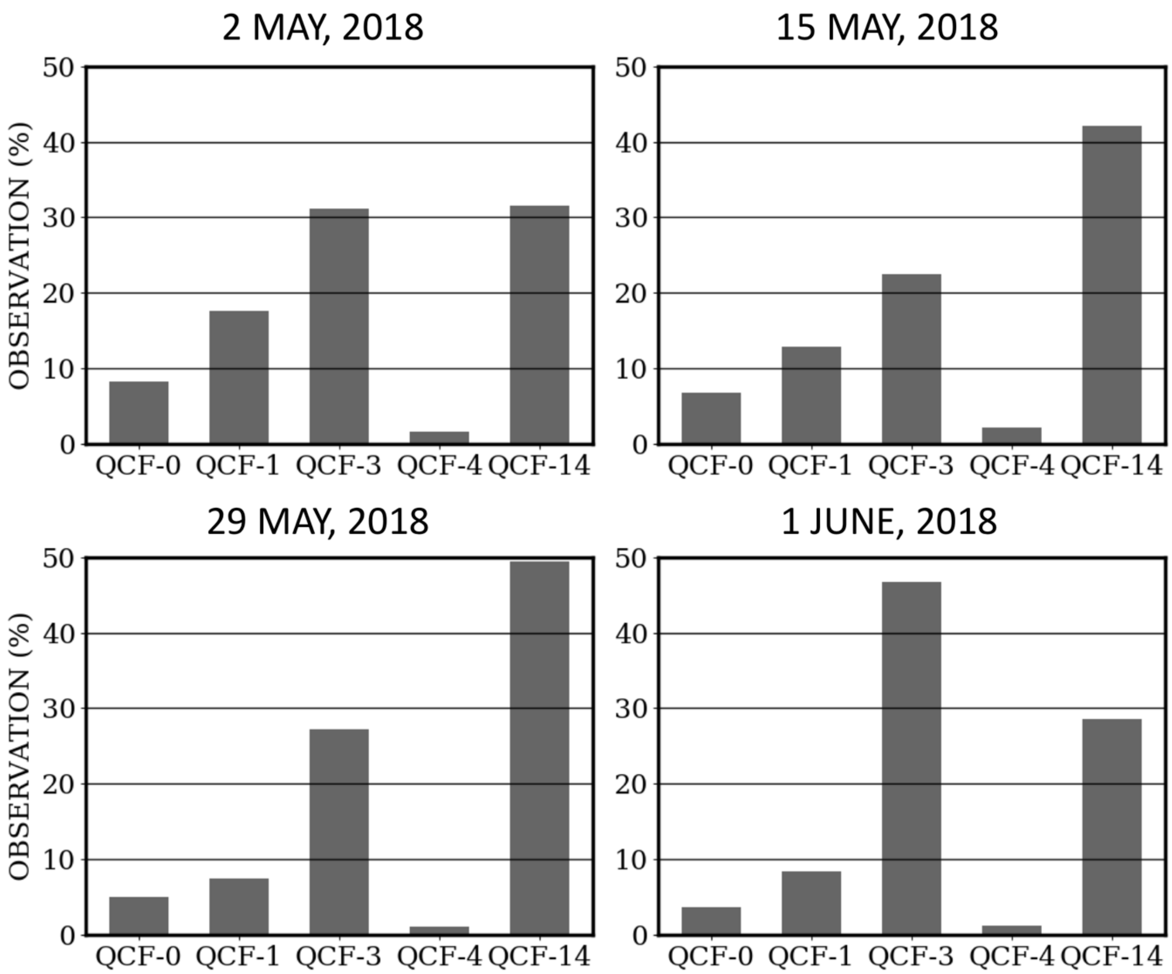

QCF-0 : Good Wind
QCF-1 : Maximum gradient below acceptable threshold
QCF-3 : Cloud amount failure
QCF-4 : Median pressure failure
QCF-14 : Height assignment

Figure 1: Percentage of AMVs available with five different quality control flag (QCF) from 1800 UTC to next day 0300 UTC. Each panel represent the convective cases considered in this study.

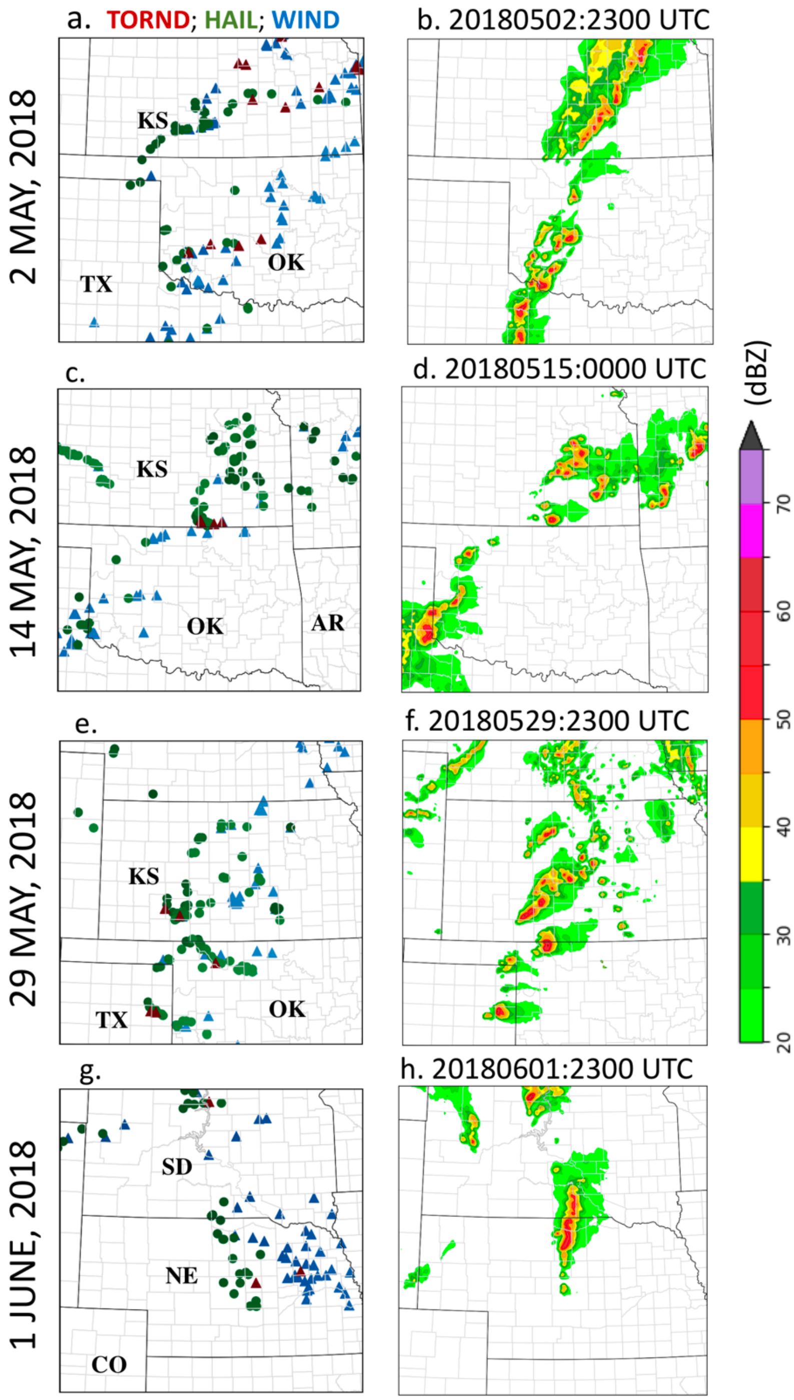

Figure 2: Location of tornado (triangle), hail (circle) and wind (triangle) reports over the model domain for each case and the Multi-Radar/Multi-Sensor System (MRMS) composite reflectivity (dBZ) for each case at a selected analysis time.

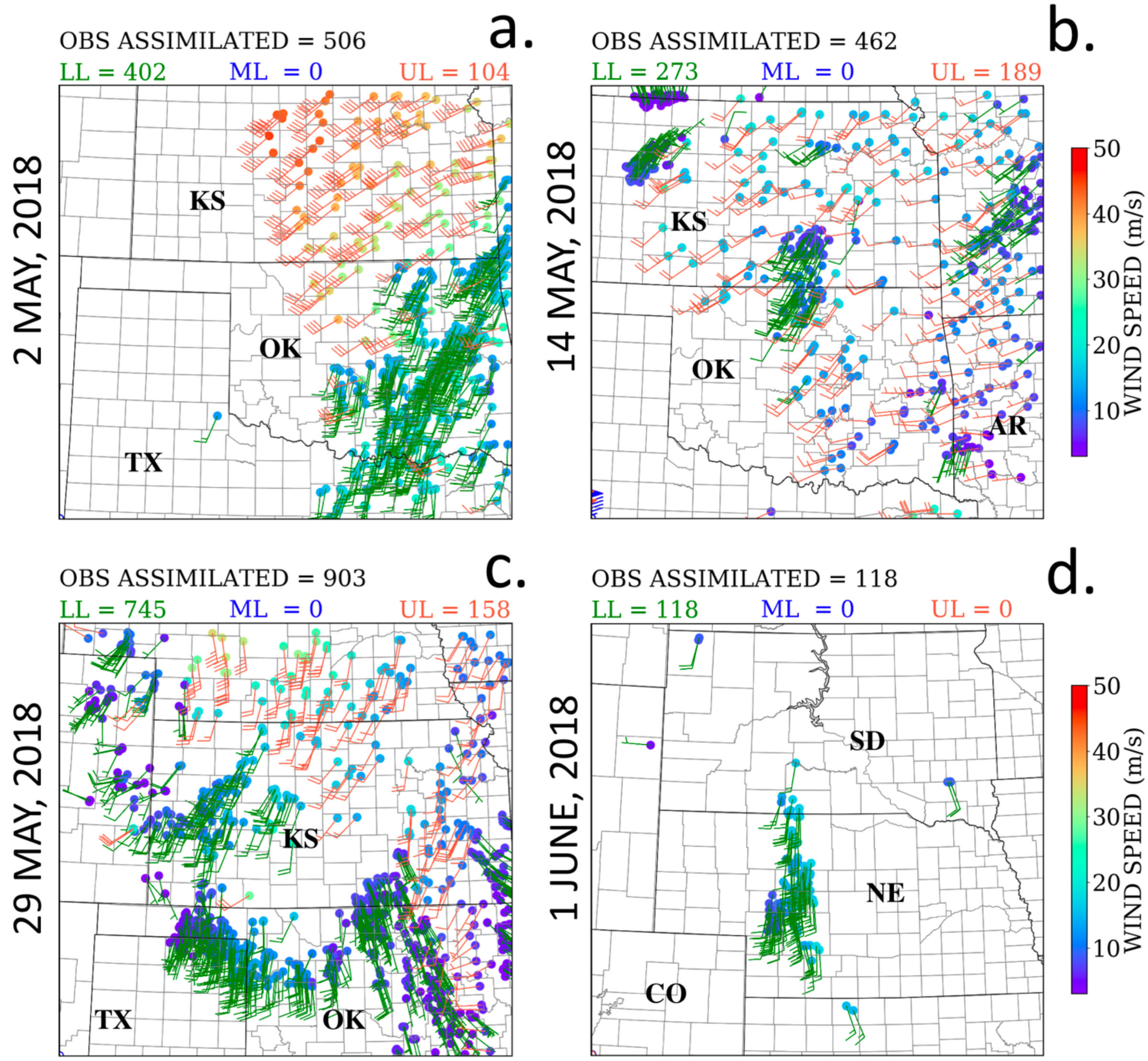

Figure 3: Spatial distribution of 1800 UTC assimilated AMVs within the study domain of each case. The numbers on the top of each panel represent total number of observations assimilated at 1800 UTC and the corresponding number of observations counted in each three different level starting from lower level (LL) from 1000-700 hPa; the middle level (ML) from 700-400 hPa and the Upper level (UL) from 400-100 hPa.

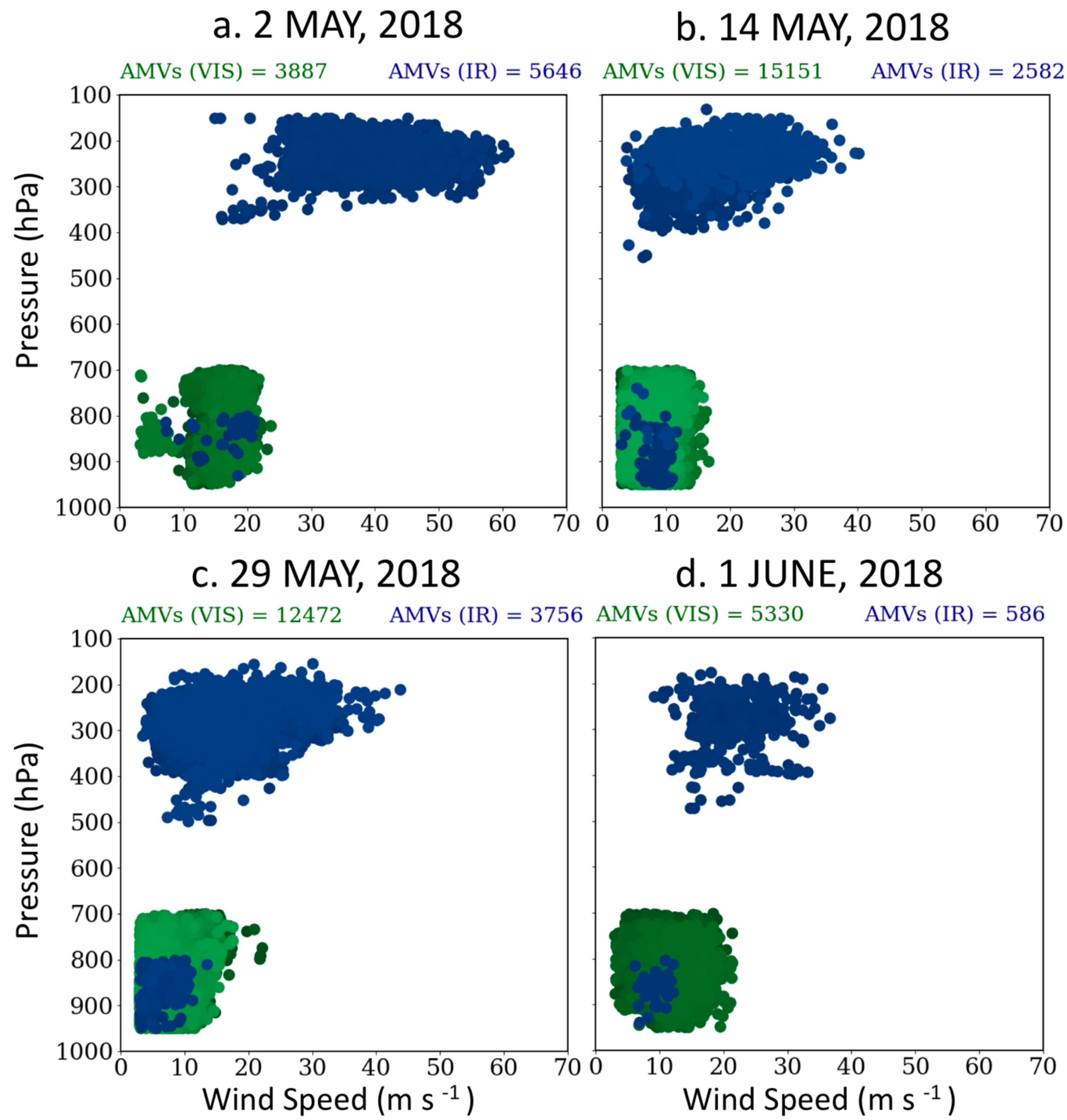

Figure 4: Scatterplot of assimilated AMVs in terms of wind speed (x-axis) at different pressure level (y-axis) from Visible and IR channels from 1800 UTC to next day 0300 UTC for each case. The green circles are from VIS and blue circle from IR channel.

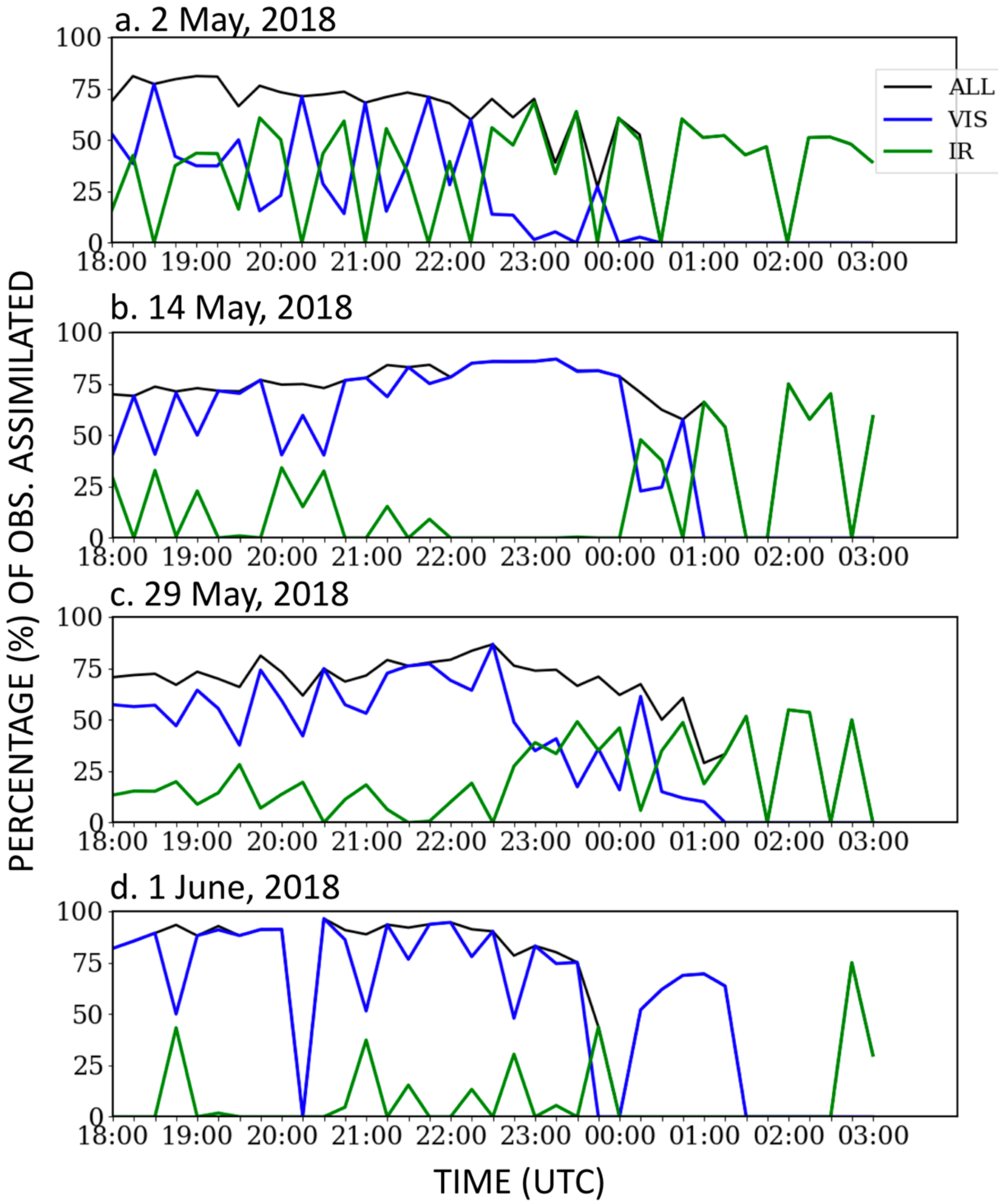

Figure 5: Percentage of observations assimilated in the WoFS at 15 min assimilation cycle from 1800 UTC to next day 0300 UTC for each event. The solid black line represents the percentage of AMVs assimilated including all VIS and IR channel, whereas the blue line is only for the VIS and the green line for IR channels. The percentage of observations is calculated between the total number of good AMVs before the two stage of QC in observation processing (QCS-1) and data assimilation step (QCS-2) with the number of the assimilated observations.

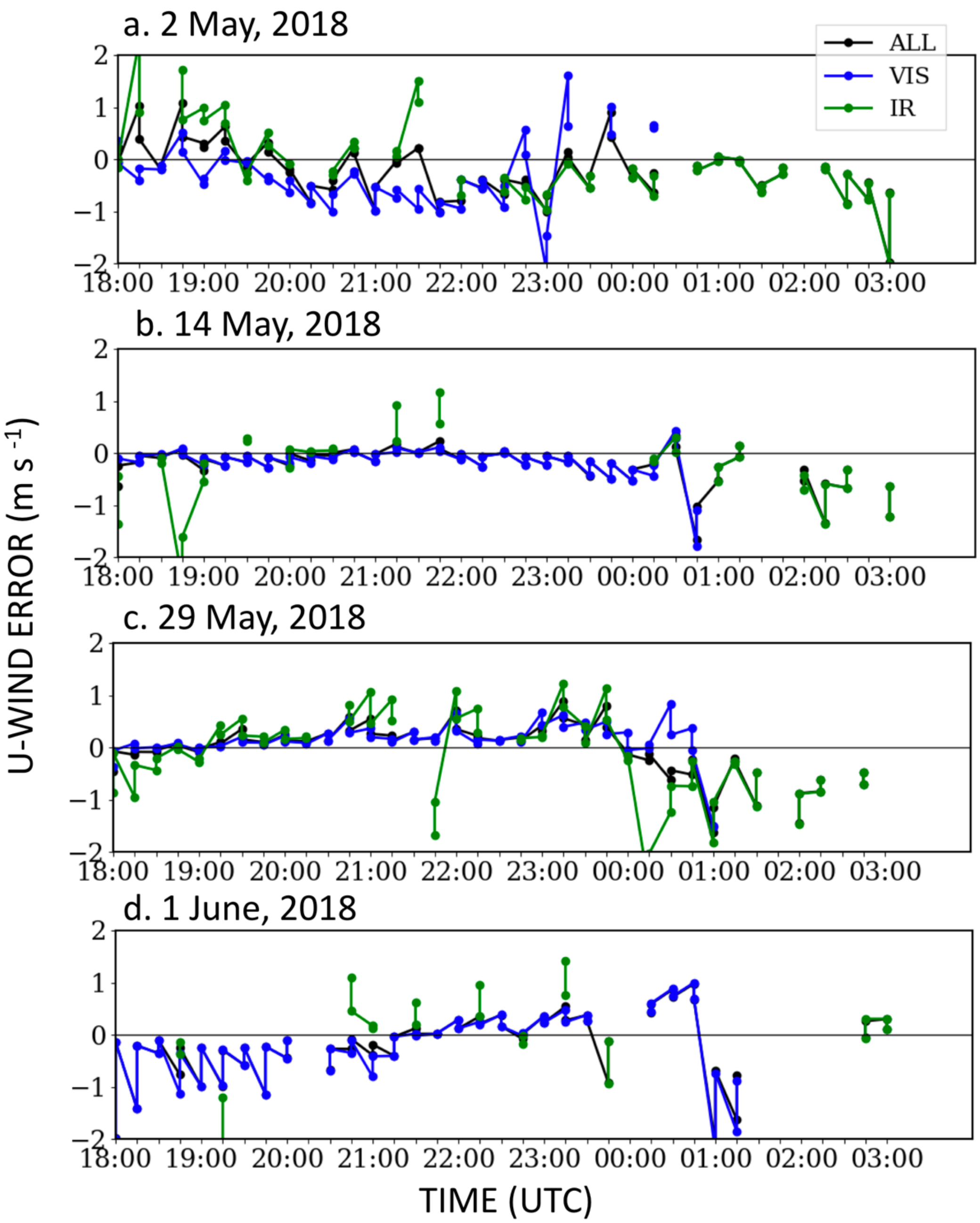

Figure 6: Ensemble mean u-wind observation innovations at 15 min assimilation cycle from 1800 UTC to next day 0300 UTC for each case. The solid black line represents the innovation of AMVs assimilated including all VIS (blue line) and IR (green line) channel.

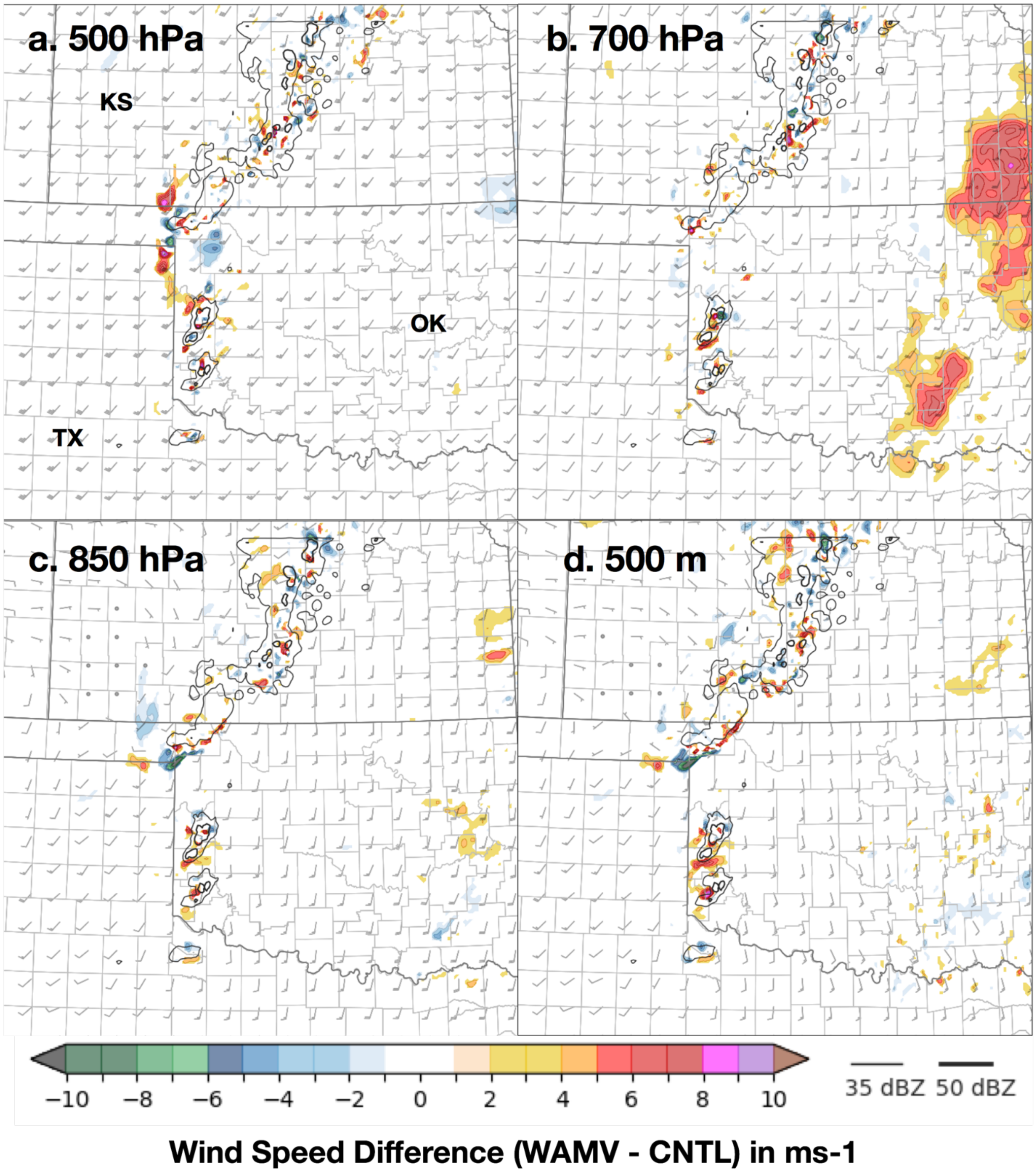

Figure 7. Analyzed ensemble mean wind speed difference (in m s^{-1}) between WAMV and CNTL at four different levels (500, 700, 850 hPa and 500 AGL) at 2100 UTC 2 May 2018. Wind barbs represent WAMV wind speed and direction at this time.

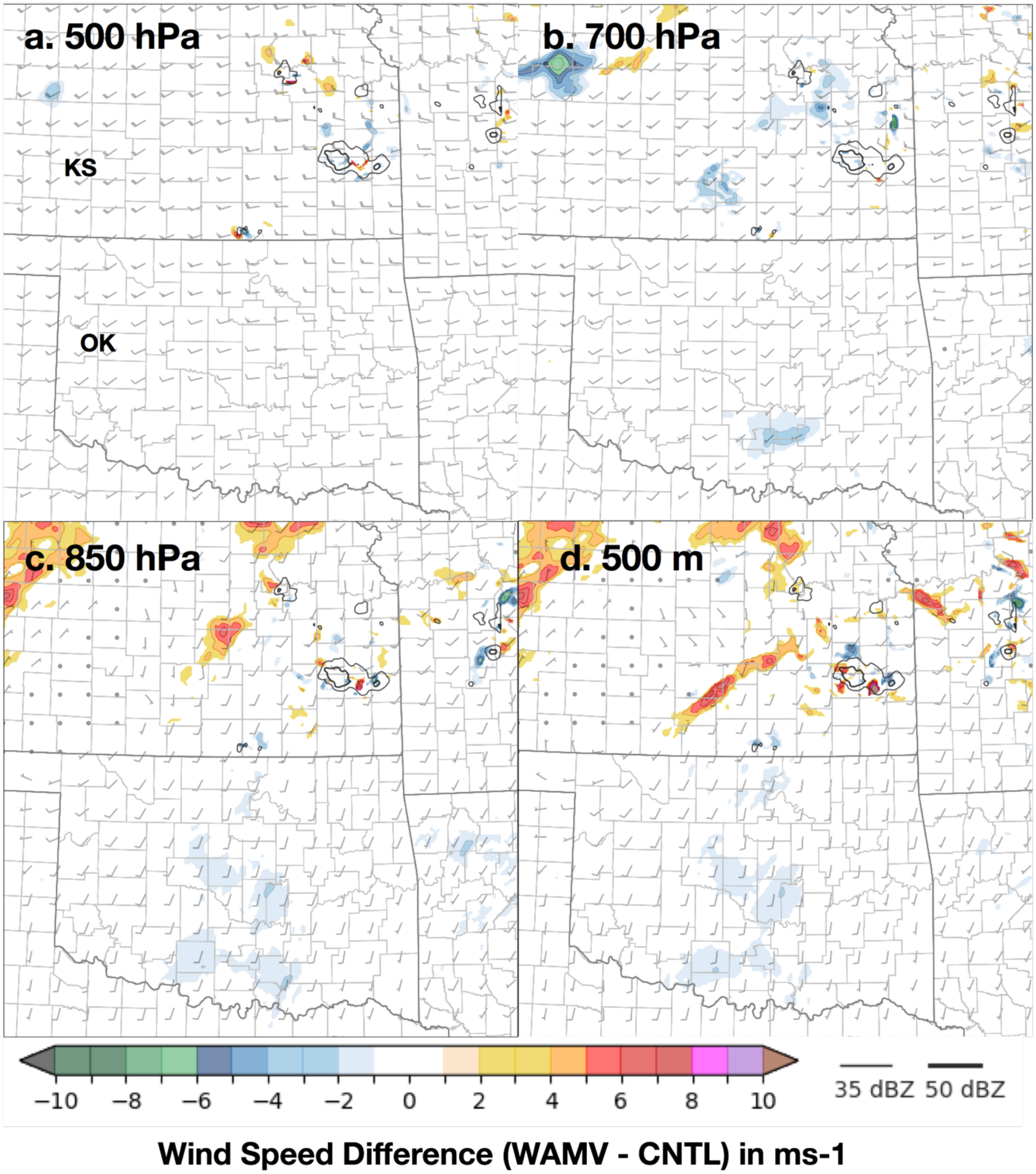

Figure 8. Same as Figure 7, but for 2100 UTC 14 May.

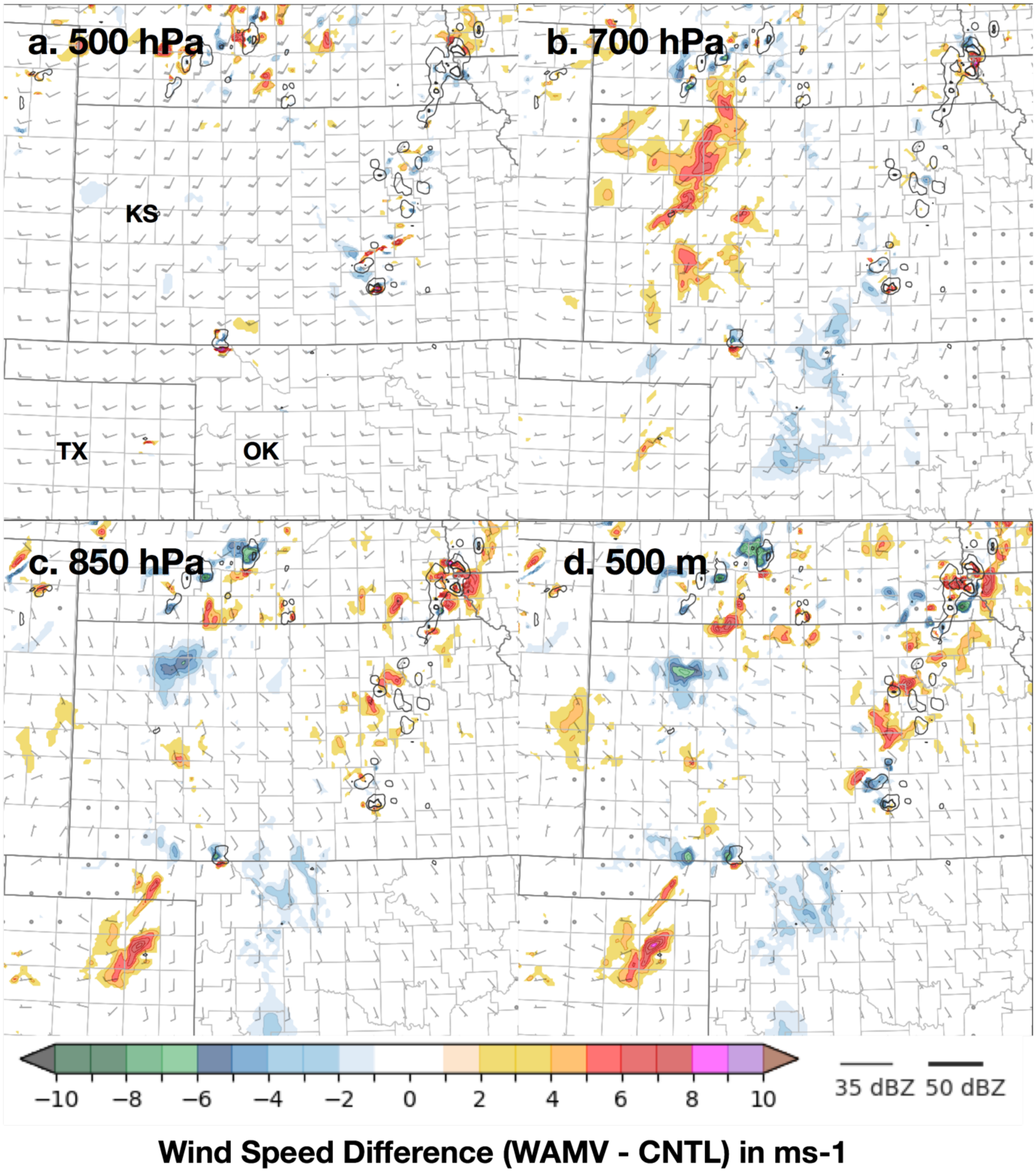

Figure 9. Same as Figure 7, but for 2100 UTC 29 May.

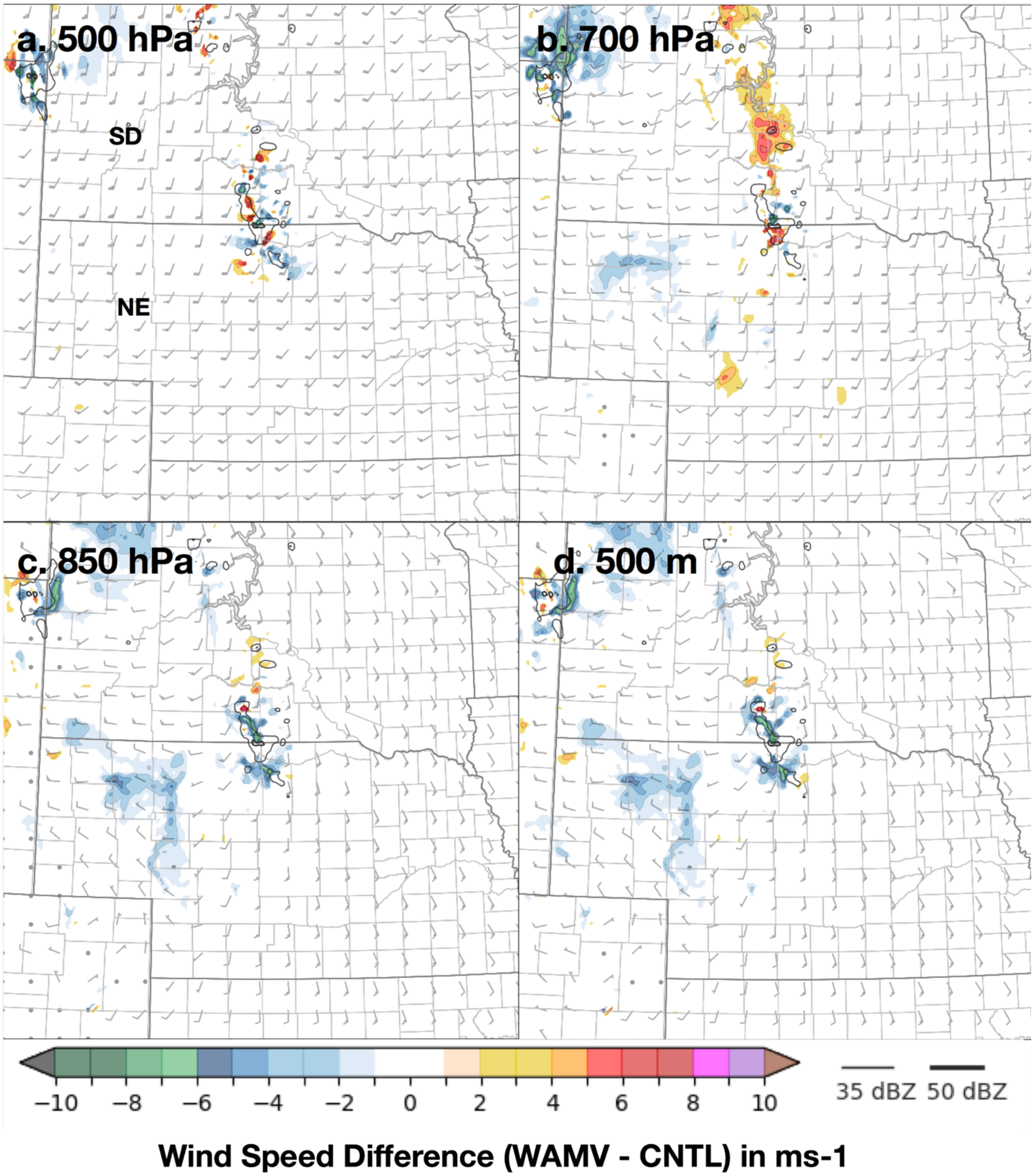

Figure 10. Same as Figure 7, but for 2100 UTC 1 June.

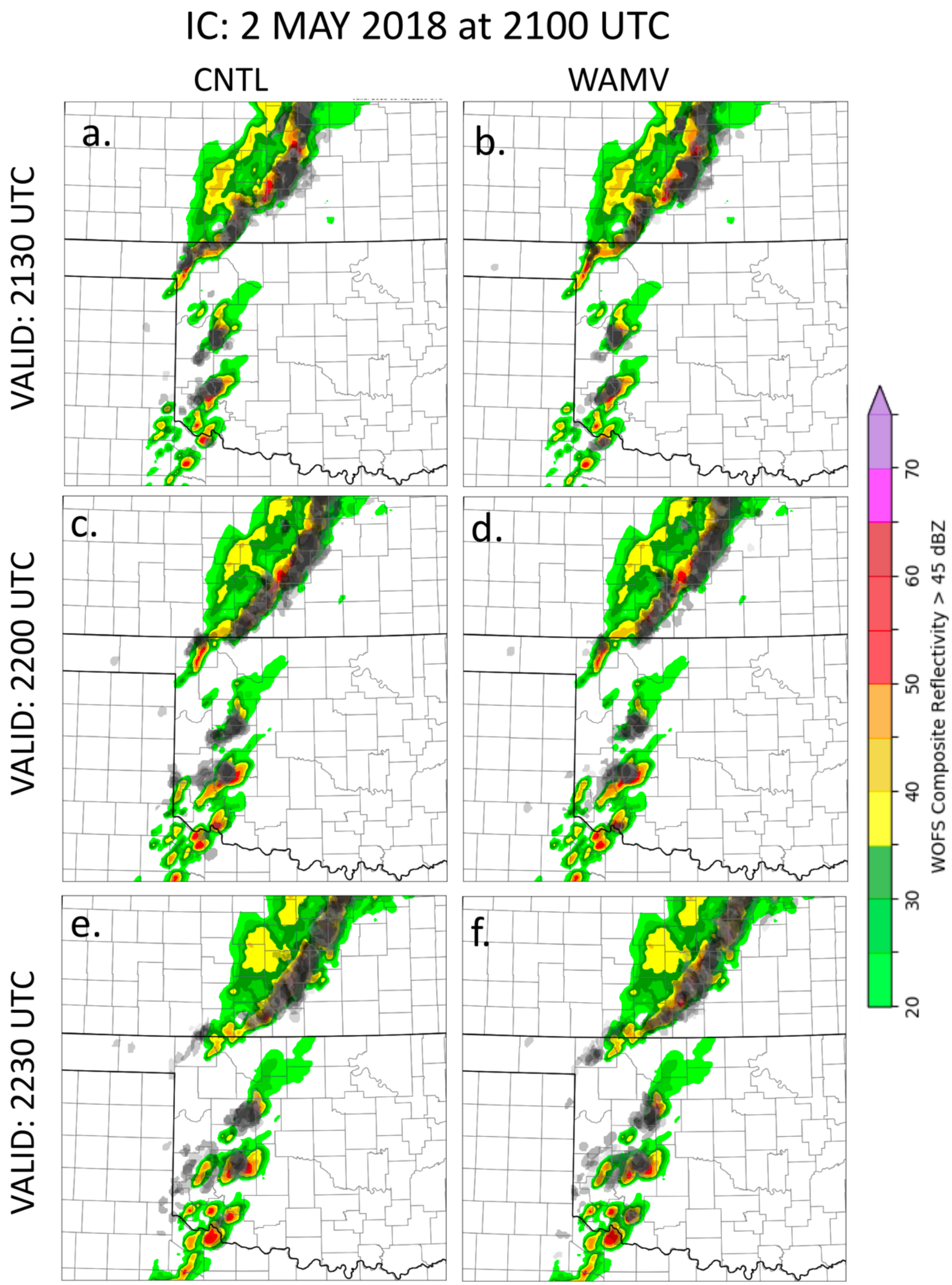

Figure 11. Forecast composite reflectivity > 45 dBZ from CNTL and WAMV initiated at 2100 UTC. Darker grays indicate more members generate convection at a particular location. Background plot shows observed WSR-88D composite reflectivity valid at the forecast time.

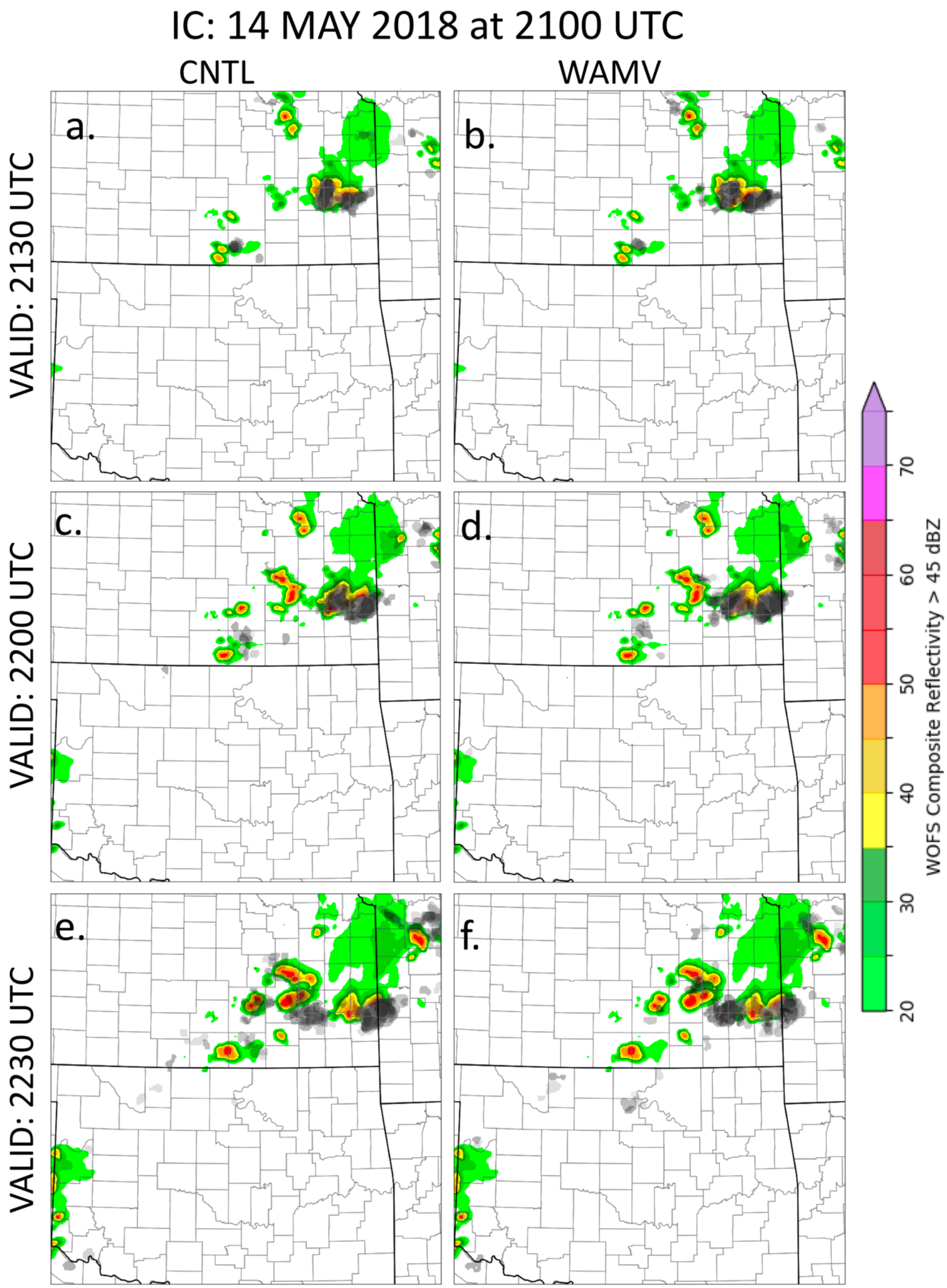

Figure 12. Same as Figure 11, but for forecasts initiated at 2100 UTC 14 May.

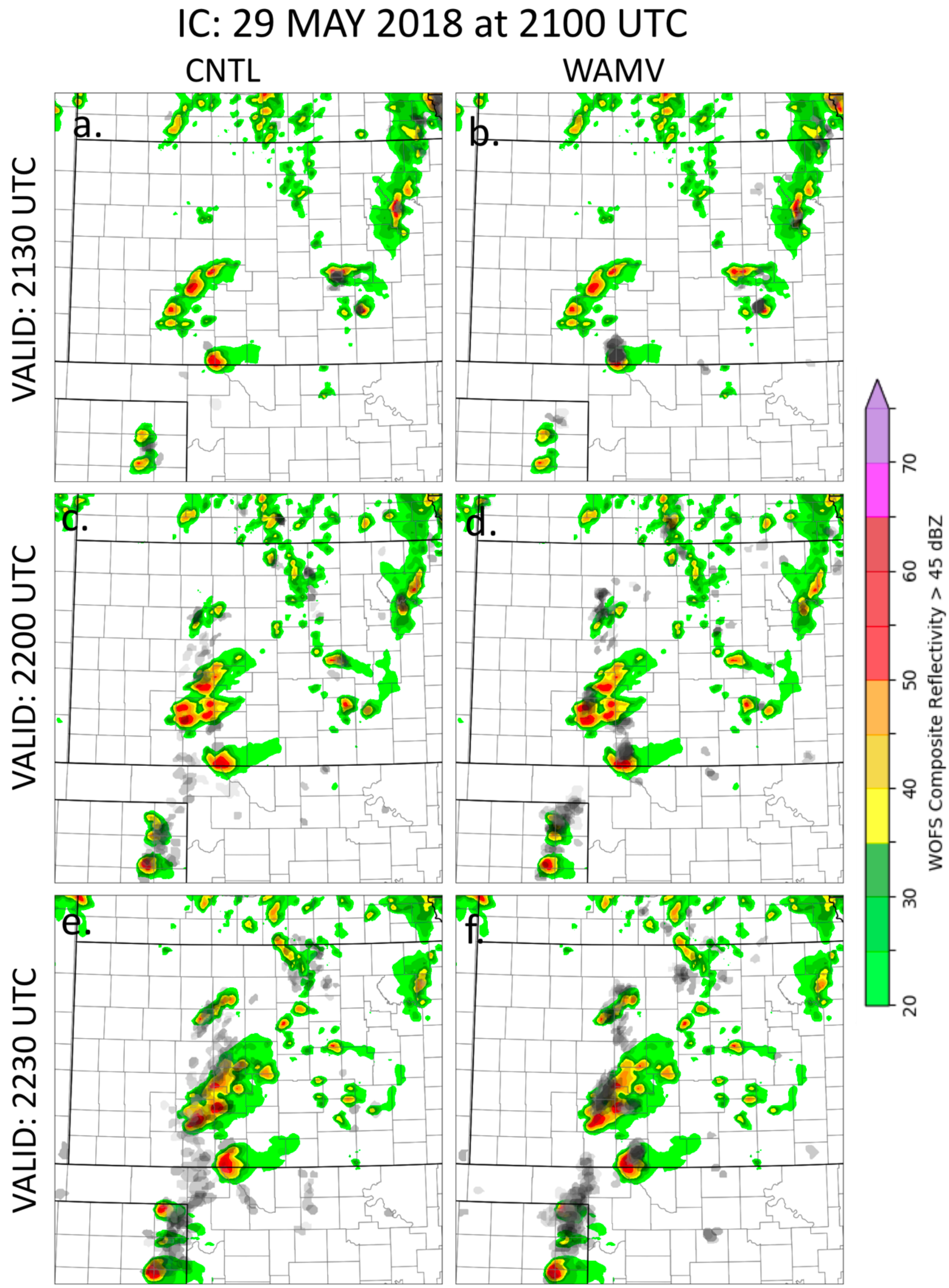

Figure 13. Same as Figure 11, but for forecasts initiated at 2100 UTC 29 May.

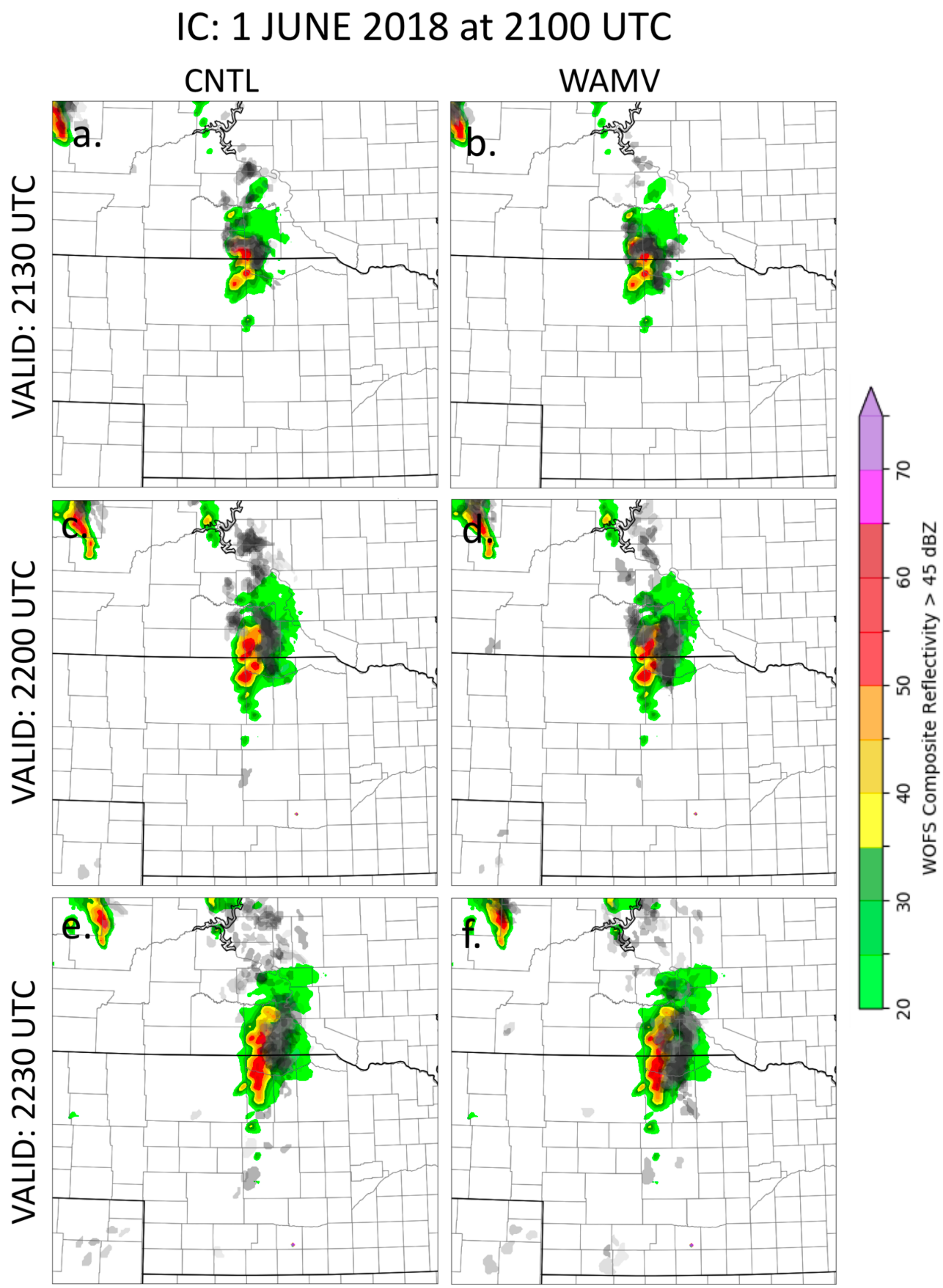

Figure 14. Same as Figure 11, but for forecasts initiated at 2100 UTC 1 June.

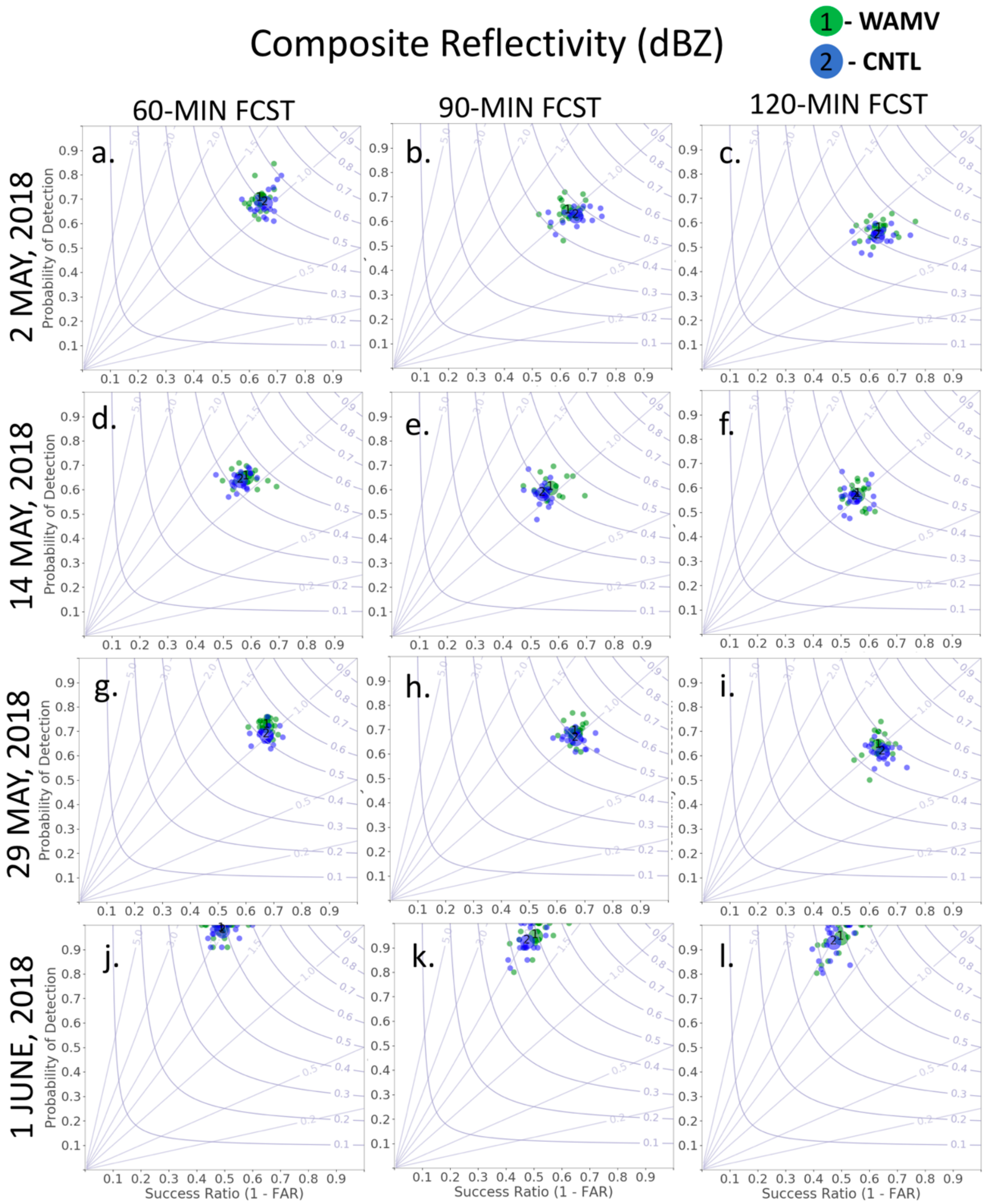

Figure 15. Performance diagram at (left) 60-min, (center) 90-min and (right) 120-min forecast time for composite reflectivity (dBZ) forecasts for 4 different cases. The two different colors in all the panels represents the two types of forecasts WAMV and CNLT. Large dots indicate ensemble mean performances while smaller dots indicate individual member performances. The maximum forecast skill is located at the top right corner and the minimum forecast skill is in the bottom left of these diagrams. For a perfect score, success ratio = 1 and probability of detection = 1. The curved lines represent critical success index (CSI), and the diagonal lines represent bias.

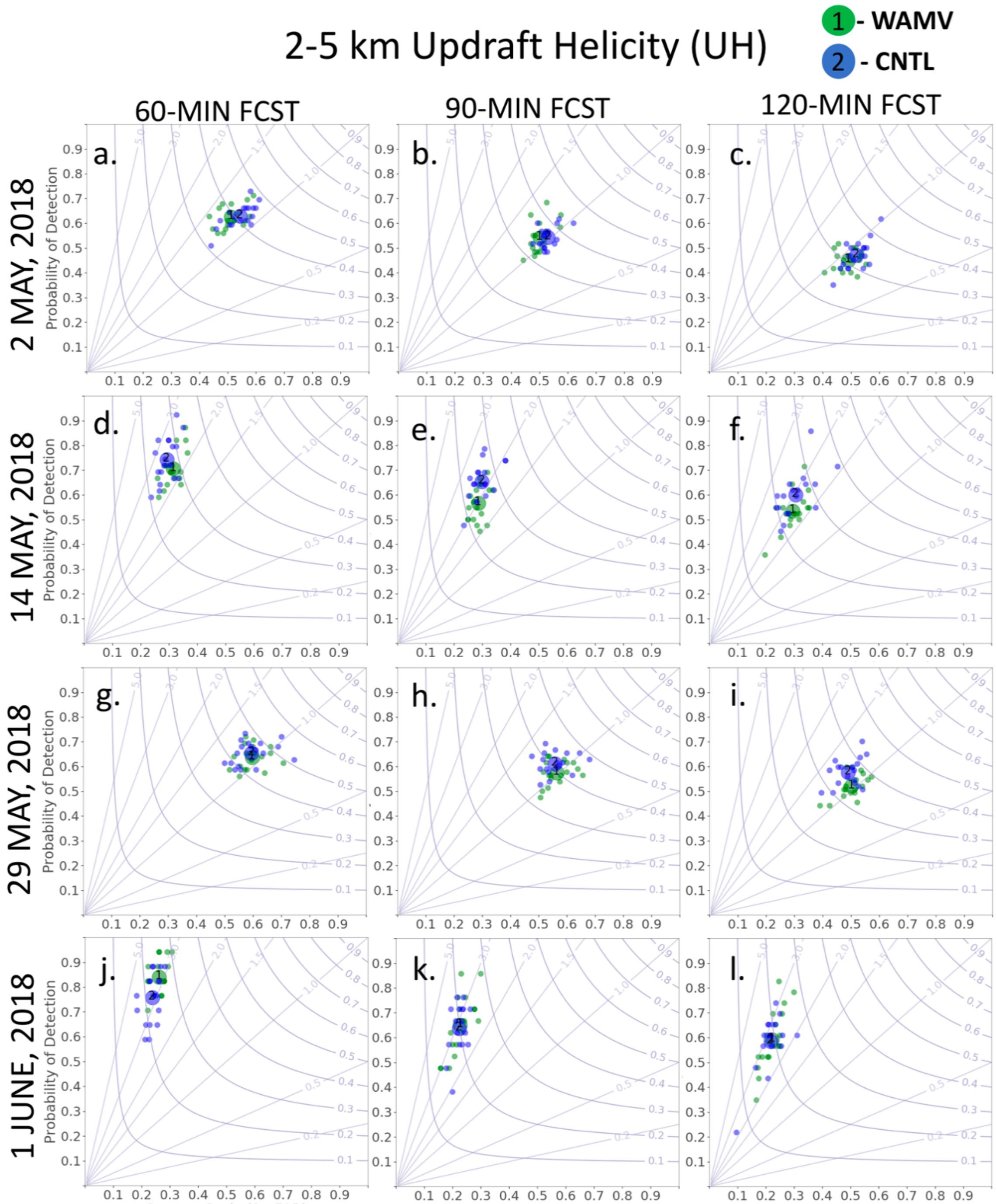

Figure 16. Same as Figure 15, but for 2-5 km Updraft Helicity (UH).